

Review

Emergent CuWO₄ Photoanodes for Solar Fuel Production: Recent Progress and Perspectives

Jin Uk Lee ¹, Jin Hyun Kim ^{2,*} and Jae Sung Lee ^{1,*}

¹ School of Energy and Chemical Engineering, Ulsan National Institute of Science and Technology (UNIST), 50 UNIST-gil, Ulsan 44919, Republic of Korea; leejuw6588@unist.ac.kr

² Laboratory of Photonics and Interfaces, Institute of Chemical Sciences and Engineering, École Polytechnique Fédérale de Lausanne, 1015 Lausanne, Switzerland

* Correspondence: jinhyun.kim@epfl.ch (J.H.K.); jlee1234@unist.ac.kr (J.S.L.)

Abstract: Solar fuel production using a photoelectrochemical (PEC) cell is considered as an effective solution to address the climate change caused by CO₂ emissions, as well as the ever-growing global demand for energy. Like all other solar energy utilization technologies, the PEC cell requires a light absorber that can efficiently convert photons into charge carriers, which are eventually converted into chemical energy. The light absorber used as a photoelectrode determines the most important factors for PEC technology—efficiency, stability, and the cost of the system. Despite intensive research in the last two decades, there is no ideal material that satisfies all these criteria to the level that makes this technology practical. Thus, further exploration and development of the photoelectrode materials are necessary, especially by finding a new promising semiconductor material with a suitable band gap and photoelectronic properties. CuWO₄ (n-type, E_g = 2.3 eV) is one of those emerging materials that has favorable intrinsic properties for photo(electro)catalytic water oxidation, yet it has been receiving less attention than it deserves. Nonetheless, valuable pioneering studies have been reported for this material, proving its potential to become a significant option as a photoanode material for PEC cells. Herein, we review recent progress of CuWO₄-based photoelectrodes; discuss the material's optoelectronic properties, synthesis methods, and PEC characteristics; and finally provide perspective of its applications as a photoelectrode for PEC solar fuel production.

Keywords: solar fuels; photoelectrochemical cell; photoelectrode; copper tungstate; water splitting



Citation: Lee, J.U.; Kim, J.H.; Lee, J.S. Emergent CuWO₄ Photoanodes for Solar Fuel Production: Recent Progress and Perspectives. *Catalysts* **2023**, *13*, 1408. <https://doi.org/10.3390/catal13111408>

Academic Editor: Akira Nishimura

Received: 23 September 2023

Revised: 23 October 2023

Accepted: 24 October 2023

Published: 30 October 2023



Copyright: © 2023 by the authors. Licensee MDPI, Basel, Switzerland. This article is an open access article distributed under the terms and conditions of the Creative Commons Attribution (CC BY) license (<https://creativecommons.org/licenses/by/4.0/>).

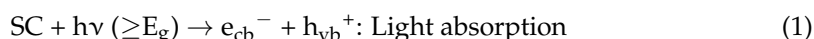
1. Introduction

The climate change due to rapidly increasing atmospheric CO₂ concentration has become an imminent threat to the sustainability of human beings' lives on earth [1]. Solar fuel production is considered an effective strategy to address this urgent global issue, which harvests solar energy and converts and stores it as chemical energy [2]. Three technologies are available for solar fuel production: the photovoltaic cell–electrolyzer (PV-EC) combination is highly efficient but expensive; particulate photocatalysis (PC) is low cost but also low efficiency; the photoelectrochemical (PEC) cell is positioned in the middle of these two technologies, having modest efficiency and cost [3,4]. All the three technologies need to be developed further to create a highly efficient but low cost practical system.

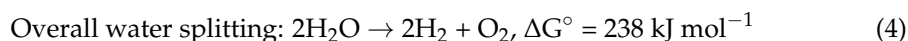
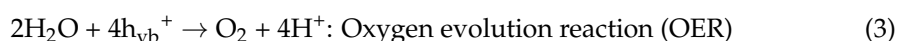
In particular, the PEC device can have a diverse configuration, ranging from a buried junction to a semiconductor–liquid junction (SCLJ) for photovoltage generation [3], and, thus, can utilize a variety of light absorber materials from PV grade materials to stabilize metal oxide semiconductors [4]. Since the long-term stability (>10 years) of aqueous electrolytes is essential for the PEC cells, SCLJ devices are the most staple and general of those used [5]. Also, fundamental studies of the charge transfer mechanism have been focused on SCLJ type PEC cells. For instance, the reaction order for PEC SCLJ water oxidation with Fe₂O₃ photoanode was found to be in the third order in respect to the

hole concentration with an activation energy (E_a) of 60 meV, which is different from those for typical electrochemical water oxidation (the first order, $E_a > 300$ mV) [6]. Such uniqueness makes further study and the development of the SCLJ PEC cell more interesting and worthwhile.

The PEC water splitting starts from the absorption of photons with energy greater than the band gap energy (E_g) of the semiconductor (SC) comprising the photoelectrode [7]:



Electrons in the conduction band (CB) (e_{cb}^-) with an energy level above 0.0 V vs. RHE diffuse to the surface and reduce water to generate hydrogen on a hydrogen evolution co-catalyst (HEC). Holes in the valence band (VB) (h_{vb}^+) with an energy level below 1.23 V vs. RHE also diffuse to the surface and oxidize water to generate oxygen, often on an oxygen evolution co-catalyst (OEC). This process leads to the overall water-splitting reaction and produces hydrogen from water using solar energy.



Theoretically, a semiconductor can split water if its E_g is greater than 1.23 eV (water dissociation energy) and its CB and VB edge energy levels are more negative and more positive than the water reduction (0.0 V_{RHE}) and oxidation (1.23 V_{RHE}) potentials, respectively [8]. In reality, a much larger E_g than 1.23 eV is needed to overcome the overpotentials of the reactions (~0.05 V for HER and ~0.25 V for OER); thus, a total >1.5 V is needed [7,8]. In addition, the rate of reaction is much smaller than the rate of light absorption because of dominant electron–hole recombination, which is the main energy loss process.

General guidelines for selecting metal oxide light absorbers that could be used as photocatalysts for water splitting have often been suggested in previous reviews [7,9,10]. Metal oxide should have adequate energy levels for VBM and CBM, as well as chemical inertness against self-oxidation and a reduction in electrolytes. The VBM is mainly composed of the O 2p orbital of bonding state, while the CBM is often composed of d^0 (Ti^{4+} , Zr^{4+} , Nb^{5+} , Ta^{5+} , V^{5+} , W^{6+} , and Ce^{4+}) and d^{10} (Zn^{2+} , In^{3+} , Ga^{3+} , Ge^{4+} , Sn^{4+} , and Sb^{5+}) compounds. However, the majority these semiconductors have large band gaps (3.0 eV~3.2 eV) and only absorb UV light. For example, titanates (TiO_2 , SrTiO_3) have proper band alignments for overall water splitting with high quantum yields, but they can only absorb UV light, which limits the solar-to-hydrogen (STH) conversion efficiency to a very low level (the reported highest value is 0.65% [11]).

This generated demand for metal oxide semiconductors that are active under visible light ($E_g < 3.0$ eV). Thus, WO_3 ($E_g = 2.8\sim 2.6$ eV) and Fe_2O_3 ($E_g = 2.1$ eV) have been extensively studied for generating photocurrent densities (J_{ph}) above 4.0 mA/cm^2 @ 1.23 V_{RHE} under one sun irradiation (100 mW/cm^2) [12].

As such a performance of the binary oxides was not satisfactory, tertiary metal oxides were introduced to form adequate electronic structures with smaller band gaps. One of the most successful cases is BiVO_4 with VBM composed of Bi 6s and O 2p, which gives a respectable E_g of 2.4 eV. With a relatively high diffusion length and charge mobility, the state-of-the art BiVO_4 photoanode records a J_{ph} above 6.0 mA/cm^2 @ 1.23 V_{RHE} , which represents the highest among all metal oxide light absorbers [13]. CuWO_4 , which is one of the photoactive ternary tungstates (Bi_2WO_6 , which showed PEC water oxidation activity [14], and ZnWO_4 , which showed pollutant degradation [15] and PEC water oxidation activity [16]), is also a tertiary metal oxide, with CBM composed of W5d and Cu3d and VBM composed of Cu 3d and O 2p, and it could be used as a photocatalyst and a photoanode for water oxidation [17,18]. Although it has a strong indirect band gap property, its smaller

band gap ($E_g = 2.3$ eV) than that of WO_3 ($E_g = 2.7$ eV) is quite attractive. Hence, here we discuss CuWO_4 's potential as an emergent photoanode material for solar fuel production.

2. CuWO_4 as a Photoanode Material

2.1. Crystal Structure of Photoactive CuWO_4

The CuWO_4 has a unique crystal structure made of distorted wolframite because W ions in WO_3 are partially replaced by Cu ions. W^{6+} ions and Cu^{2+} ions are coordinated with O^{2-} ions in octahedral sites (Figure 1a). This structure has a space group of P1^- under low pressure at room temperature, with $a = 4.694 \text{ \AA}$, $b = 5.830 \text{ \AA}$, $c = 4.877 \text{ \AA}$, $\alpha = 91.64^\circ$, $\beta = 92.41^\circ$, and $\gamma = 82.91^\circ$. It is influenced by the Jahn–Teller effect caused by Cu^{2+} ions. This effect leads to distortions in the $[\text{CuO}_6]$ octahedral clusters, resulting in d orbital splitting and the breaking of the degeneracy of σ -antibonding orbitals. The unpaired electron in the $d_{x^2-y^2}$ orbital of Cu^{2+} ions, as dictated by the Pauli exclusion principle, creates a mid-gap band state, with greater stabilization observed in Jahn–Teller-elongated Cu^{2+} ions, where the $3d_{z^2}$ orbital contains two electrons [19,20].

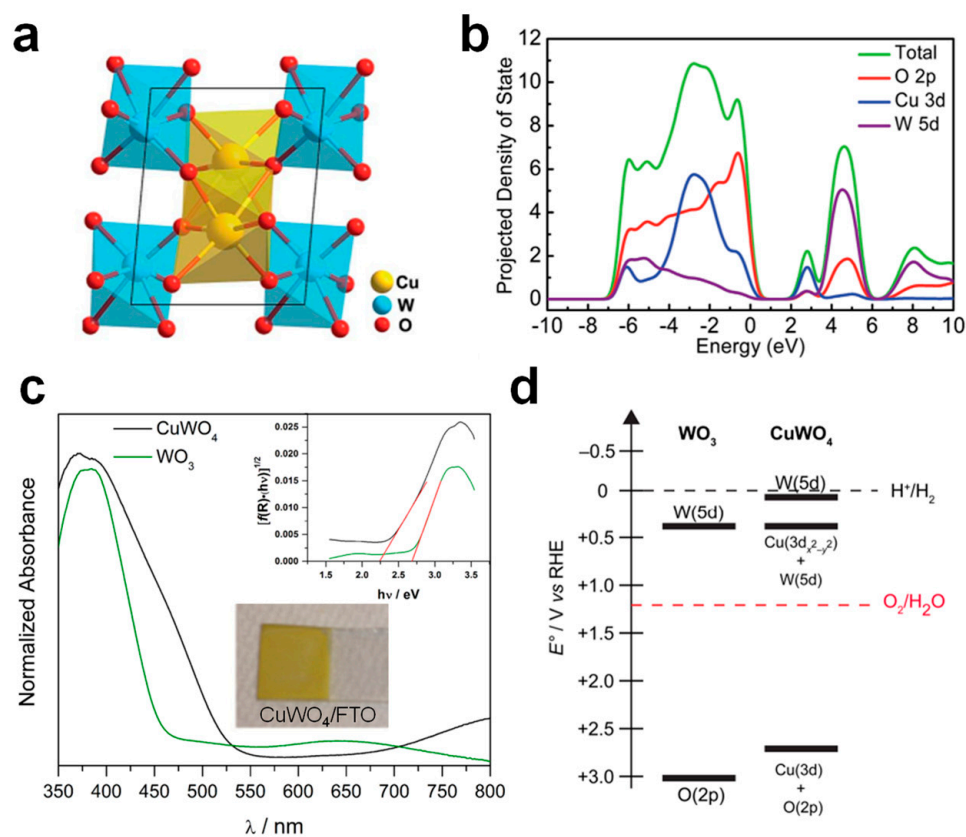


Figure 1. (a) Crystal and electronic structure of photoactive CuWO_4 . (b) Crystal structure of triclinic wolframite CuWO_4 and its calculated projected density of state using hybrid DFT, reproduced from ref. [18]. (c) UV–vis spectrum of WO_3 and CuWO_4 thin film (inset 1: picture image of CuWO_4/FTO) (inset 2: Tauc plot of WO_3 and CuWO_4 with trend line for optical direct band gap), (d) experimentally determined electronic structure of WO_3 and CuWO_4 thin film made via electrodeposition and thermal conversion on FTO, reproduced from ref. [21].

2.2. Electronic Structure of Photoactive CuWO_4

The electronic structure of CuWO_4 was elucidated via various spectroscopies and density functional theory (DFT) calculations. The conduction band is primarily characterized by the contribution from Cu 3d orbitals, with the additional participation of W 5d orbitals. Conversely, the valence band exhibits a strong hybridization between O 2p and Cu 3d orbitals, as illustrated in Figure 1b. Thus, CuWO_4 has a suitable band position for

water oxidation, an indirect band gap of 2.3~2.4 eV (Cu 3d → Cu 3d), and a direct band of 2.6~2.7 eV (O 2p → Cu 3d). Its UV-vis spectrum features an absorption onset around 550 nm, reflecting a band gap energy of 2.3 eV (Figure 1c,d). A gradual rather than sharp absorption onset is characteristic of an indirect band gap. Such an indirect band gap tends to limit the light harvesting efficiency of CuWO₄. The absorptivity coefficient α is markedly high at 6600 cm⁻¹ at 400 nm, but it drops rapidly to 1715 cm⁻¹ when the wavelength increases to 500 nm [18,20].

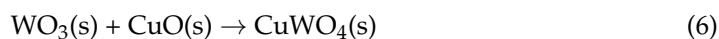
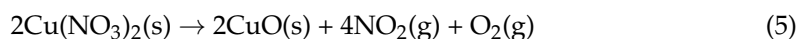
WO₃ and CuWO₄ share similar electronic structures, though a distinctive feature arises in their indirect band gaps. The CuWO₄ possesses an indirect band gap 0.4 eV narrower than that of WO₃. This smaller band gap allows CuWO₄ to absorb longer-wavelength visible light photons, as shown in Figure 1c. The increased spectral absorption is reflected in the theoretical solar-to-hydrogen (STH) conversion efficiency of CuWO₄ higher than 10%. However, the characteristics of the Cu 3d state in CuWO₄ result in electron localization, which leads to a constraint in electronic properties, specifically a charge-carrier mobility in the order of $\sim 6 \times 10^{-3}$ cm² V⁻¹ s⁻¹ and a diffusion length restricted to approximately 30 nm for photo-excited electrons in the CB. Such limitations inherently hinder the performance of CuWO₄ photoanodes, causing a substantial divergence from their theoretical efficiency. Furthermore, CuWO₄ exhibits commendable chemical and thermal stability in neutral electrolytes. This notable stability underscores the material's potential for use in various technological applications [22,23].

3. Synthesis Chemistry and Photoelectrochemical Stability

3.1. Synthesis of CuWO₄ Thin Film

J. E. Yourey et al. [21] initially presented CuWO₄ as a promising photoanode material in 2011. The material was synthesized through electrodeposition (ED) using an acidic bath containing a mixture of copper and tungsten. The ED method involved potential sweeps from +0.3 V to -0.5 V, carried out over six cycles. The subsequent annealing of this film was conducted at 500 °C for 2 h. This sample showed 0.2 mA/cm² at 1.23 V_{RHE} in 0.1 M KPi under one sun illumination. Then, J. C. Hill and K. S. Choi [14] produced CuWO₄ with an enhanced surface area by depositing an excess of Cu precursor onto electrochemically deposited porous WO₃ electrodes. This approach was found to be adaptable for other tungstate materials. The CuWO₄ films were thermally treated at 550 °C in air for 6 h and then immersed in a highly acidic solution to purify the deposited samples. This treatment resulted in an 8-micrometer thick film composed of nanoscale CuWO₄ particles, attributed to the presence of the thick underlying WO₃ film. It was ascertained that a high-temperature annealing process is vital to produce films that are both impurity-free and highly crystalline. They measured the PEC performances under varying pH conditions—strong acid (0.05 M H₂SO₄), neutral (0.1 M phosphate buffer), and weak alkaline conditions (0.1 M borate buffer)—to observe the highest J_{ph} of 0.13 mA/cm² at 1.23 V_{RHE} under weak alkaline conditions.

A different method of CuWO₄ synthesis was introduced by D. Hu et al. [24] using a solid-phase reaction with thermal assistance, circumventing the need for electrochemical procedures. The WO₃ nanoflakes (NFs) fabricated through a hydrothermal method served as a sacrificial template for the CuWO₄ synthesis. An aqueous solution of Cu(NO₃)₂ was meticulously drop-cast onto these WO₃ nanoflake arrays and subsequently allowed to dry at a moderate temperature. The detailed fabrication procedure of the CuWO₄/FTO photoanode is illustrated in Figure 2a. The transformation of the WO₃ and Cu(NO₃)₂ mixture into CuWO₄ was proposed to proceed through the following reactions:



Upon the conclusion of this thermal process, a gray–yellow composite film of CuO and CuWO₄ was produced. The residual CuO was effectively removed by submerging the

film in a 0.5 M HCl solution for 30 min, yielding a vivid yellow film. The X-ray diffraction (XRD) analysis initially showed a distinct monoclinic WO_3 pattern in a film, with specific diffraction peaks at 23.3° and 24.5° , as shown in Figure 2b. However, following a solid-phase reaction at 550°C for 2 h and the elimination of excess CuO at the surface, the WO_3 pattern disappeared completely, being replaced by a clear XRD pattern of triclinic CuWO_4 . This suggests the complete transformation of WO_3 into CuWO_4 at a lower temperature of 550°C . Figure 2c exhibits representative SEM images of the resultant CuWO_4 film, exhibiting that the flake nanostructure inherent to the WO_3 template is mostly preserved. Notably, the synthesized CuWO_4 NFs were slightly thicker than the original WO_3 NFs. They claimed that this small alteration in thickness could be attributed to the thermal treatment and the solid-phase interaction between CuO and WO_3 . Owing to their distinctive morphological and crystalline properties, the CuWO_4 NF films demonstrated higher PEC activity in comparison to previously reported CuWO_4 synthesized via the ED method. Such a distinctive structure with a vast surface area would minimize hole transport distance from within CuWO_4 to its interface and reduce the grain boundary concentration. A comparative study of CuWO_4 NF films prepared under diverse annealing durations revealed that the sample annealed at 550°C for 2 h showed the best performance, registering a photocurrent of 0.32 mA/cm^2 at $1.23\text{ V}_{\text{RHE}}$ in a 0.1 M NaBi buffer, as shown in Figure 2c. Z. Zhang et al. [25] studied the hydrothermal synthesis of CuWO_4 films on FTO substrates using a seeding layer at a moderate temperature. Using a tungsten-rich reaction solution led to a WO_3 - CuWO_4 composite film, which displayed enhanced PEC performance due to improved charge separation.

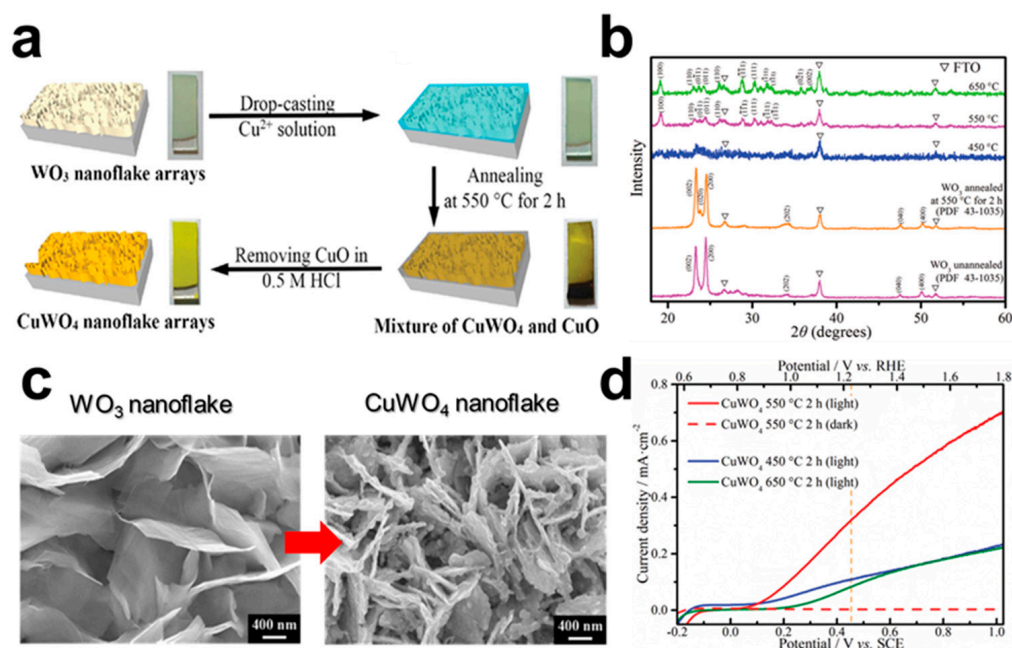


Figure 2. Solid-state reaction of WO_3 into CuWO_4 thin film. (a) Schematic illustration of the preparation procedure of the CuWO_4 NF array film on an FTO substrate. Optical images represent a WO_3 film, a WO_3 film drop-cast with $\text{Cu}(\text{NO}_3)_2$ solution, a mixture film of CuWO_4 and CuO, and a CuWO_4 film. (b) XRD pattern of CuWO_4 film annealed at 450°C , 550°C , and 650°C . (c) SEM images of the WO_3 and CuWO_4 nanoflakes prepared at 550°C for 2 h and (d) IV curve of CuWO_4 nanoflake photoanode (0.1 M NaBi buffer, pH 9.0) under one simulated sun. Reproduced from ref. [24].

C. M. Tian et al. [18] presented a solution-based synthesis approach that produced thick, high-quality, and polycrystalline CuWO_4 films. These films had distinct optoelectronic characteristics and a notable J_{ph} of $\sim 0.5\text{ mA/cm}^2$ at $1.23\text{ V}_{\text{RHE}}$. Later, J.U. Lee et al. [26] developed a greenish, transparent CuWO_4 polycrystalline film on FTO using a spin coating method, followed by annealing at 550°C for 2 h. This synthesis protocol

and optical images are shown in Figure 3a,b. The absorption spectrum of the three-layered CuWO_4 film in Figure 3c exhibits an absorption edge extended to 510 nm. The Tauc plots reveal indirect and direct band gaps of 2.43 eV and 2.89 eV, respectively, which are similar to the existing literature on polycrystalline CuWO_4 films. Moreover, the XRD for the three-layered CuWO_4 electrodes in Figure 3d clearly displays the peaks associated with the triclinic CuWO_4 phase. The surface and cross-sectional images of the CuWO_4 film observed via SEM in Figure 4d exhibit a worm-like grain morphology, forming a porous structure with an approximate thickness of 650 nm and feature sizes of 100–200 nm (Figure 4e) [26]. M.J.d.S. Costa et al. [27] compared various binary metal tungstates (AWO_4 , $\text{A}^{2+} = \text{Fe}, \text{Cu}, \text{Ni}, \text{and Co}$) as photoanode materials synthesized via a sol-gel method using a complexation of metal alkoxides and an esterification/polymerization reaction. Among AWO_4 materials, CuWO_4 showed the best PEC oxidation performance, recording a J_{ph} of $30 \mu\text{A}/\text{cm}^2$ @ 0.6 Ag/AgCl, while the position of the flat band potential (E_{fb}) related to photovoltage was the lowest. X. Duan et al. [28] reported a controllable fabrication method of ultrathin CuWO_4 films via an automatic ultrasonic spray pyrolysis method. They extensively explored the effects of varying tungsten sources and film thicknesses on the photoelectrochemical (PEC) performances of the synthesized CuWO_4 films. In particular, a CuWO_4 film derived from ammonium meta tungstate with a thickness of approximately $2.16 \mu\text{m}$ demonstrated the best PEC performance ($41 \mu\text{A}/\text{cm}^2$ at $1.23 V_{\text{RHE}}$). Then, N. Gaillard et al. [29] reported nanocomposite CuWO_4 thin films produced using spray pyrolysis from solutions of copper acetate, ammonium meta tungstate, and MWCNT, resulting in porous, crack-free polycrystalline CuWO_4 films with nanoparticle sizes of 10–50 nm. The electrochemical impedance (EIS) tests under one sun illumination showed a 30% reduction in bulk resistance for nanocomposite CuWO_4 photoanodes compared to the bare one. The CuWO_4 nanocomposite revealed improved a J_{ph} of $0.38 \text{ mA}/\text{cm}^2$ at $1.63 V_{\text{RHE}}$ in a pH 10 buffer, and MNCNT acted as effective electron collectors throughout the CuWO_4 bulk.

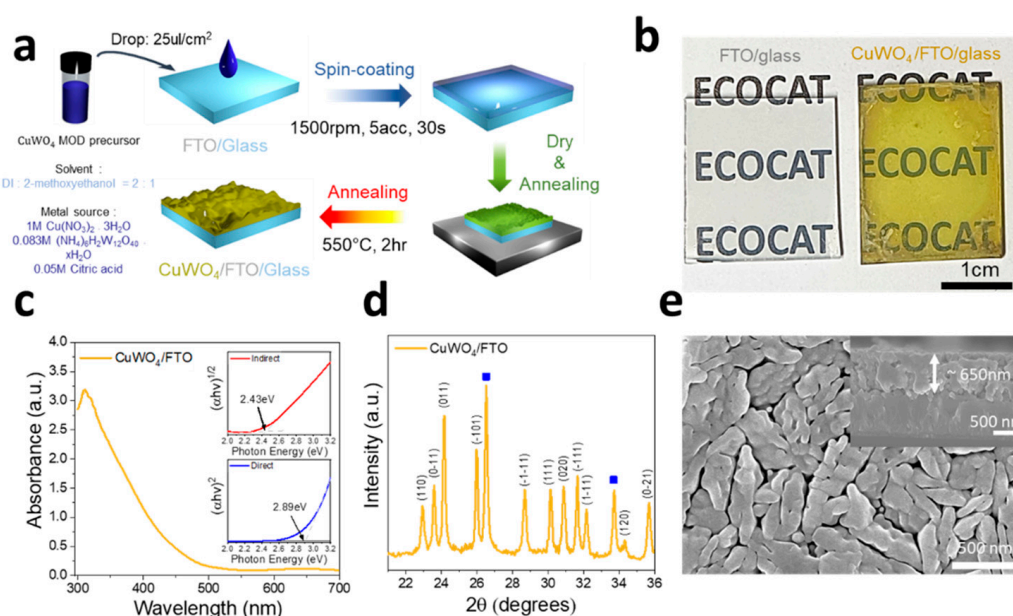


Figure 3. Polycrystalline CuWO_4 film synthesized via a sol-gel coating method: (a) schematics of CuWO_4 film coatings on FTO using 1.0 M Cu and W precursors, (b) optical images of the films, (c) UV-vis spectrum and Tauc plot (insets), (d) XRD pattern (blue square indicates pattern of FTO, F doped SnO_2 as substrate), and (e) a SEM image of CuWO_4/FTO . Reproduced from ref. [26].

Meanwhile, Y. Gao et al. [30] fabricated CuWO_4 with a Cu:W ratio of 1:1 via the atomic layer deposition method. Subsequent annealing at $600 \text{ }^\circ\text{C}$ for 30 min facilitated a solid-state reaction between CuO and WO_3 , resulting in CuWO_4 films with elaborately

controlled thicknesses and compositions. This CuWO_4 showed 0.11 mA/cm^2 at $1.23 V_{\text{RHE}}$ in $0.2 \text{ M pH } 9 \text{ KCl}$. The chemical vapor deposition method was applied by D. Peeters et al. [23] as another synthesis method that makes it easy to control the stoichiometry of Cu and W in CuWO_4 by employing $[\text{Cu}(\text{etaoac})_2]$ and $[\text{W}(\text{NtBu})_2(\text{dpamd})_2]$ precursors. By manipulating process parameters, they varied Cu-to-W ratios, enabling in-depth studies of the effects of stoichiometry on optical and PEC properties. The CuWO_4 of Cu:W = 1:1 showed the best performance ($J_{\text{ph}} = 0.06 \text{ mA cm}^{-2}$) at $1.23 V_{\text{RHE}}$ under frontside one sun illumination.

C. M. Gonzalez et al. [31] proposed pulsed laser deposition (PLD) onto an insulating substrate for synthesizing CuWO_4 thin films. They investigated the temperature dependence of electronic conductivity for CuWO_4 films across the $100\text{--}500 \text{ }^\circ\text{C}$ temperature range. Although they did not measure the PEC performance, they showed that CuWO_4 can be synthesized via PLD. A. Hrubantova et al. [32] made CuWO_4 films via reactive high-power impulse magnetron sputtering (HiPIMS) in an argon/oxygen gas mixture using two pieces of magnetron for Cu and W. They observed that both the composition and crystal structure of the as-deposited and post-annealing films depended on the deposition conditions. The samples synthesized on the FTO compromised the WO_3 and CuWO_4 or Cu_2WO_4 phases.

Thus, CuWO_4 photoanodes can be synthesized via a variety of methods, but none of them has distinguished itself through outstanding PEC performance. Further exploration of more effective synthesis methods is in order.

3.2. Stability of CuWO_4

A fundamental requirement for photoelectrodes is their chemical stability in aqueous solutions under light irradiation. The photostability of CuWO_4 photoanodes was assessed in comparison to WO_3 (Figure 4a,b) in different electrolytes (KPi and KBi buffer, pH 7) (Figure 4c–f). In KBi buffer at pH 7, CuWO_4 photoanodes exhibited remarkable stability, maintaining 93% of their initial photocurrent density over a 12-h period. Conversely, in KPi buffer of the same pH, the photocurrent experienced a 50% decline within the initial 4 h and further deteriorated to only the 15% level after a 12-h period. This stark difference implies that the phosphate anion impairs the stability of CuWO_4 in aqueous solutions. The CuWO_4 electrodes also were tested under higher irradiance conditions to evaluate the degradation of the electrode. The rate of electrode degradation increased in all buffer solutions. The overall trend remained the same, with CuWO_4 photoanodes exhibiting better stability in the KBi buffer compared to the KPi buffer.

The CuWO_4 photoanodes exhibit a faradic efficiency approaching unity for water oxidation in an equimolar KBi and NaCl solution at pH 7, underscoring their potential utility in this application. In particular, the chronoamperometry (j-t) profiles for 0.1 M KBi and 0.1 M KBi with 100 mM NaCl remain stable under irradiation of both 100 and 1000 mW/cm^2 . In contrast, WO_3 begins to dissolve within the initial 30 min of illumination. After a 12-h soaking in KPi electrolyte, the WO_3 film displayed a substantial reduction in photocurrent from 0.17 to 0.03 mA/cm^2 . This enhanced stability of the CuWO_4 film arises from a boosted covalency in Cu-O bonds, which hinders the acid–base reaction in WO_3 at $>\text{pH } 5$. Moreover, such stability is preserved during water splitting, which is distinctly different to the WO_3 case that generates peroxy intermediates during the reaction, thus hastening its degradation [17,21].

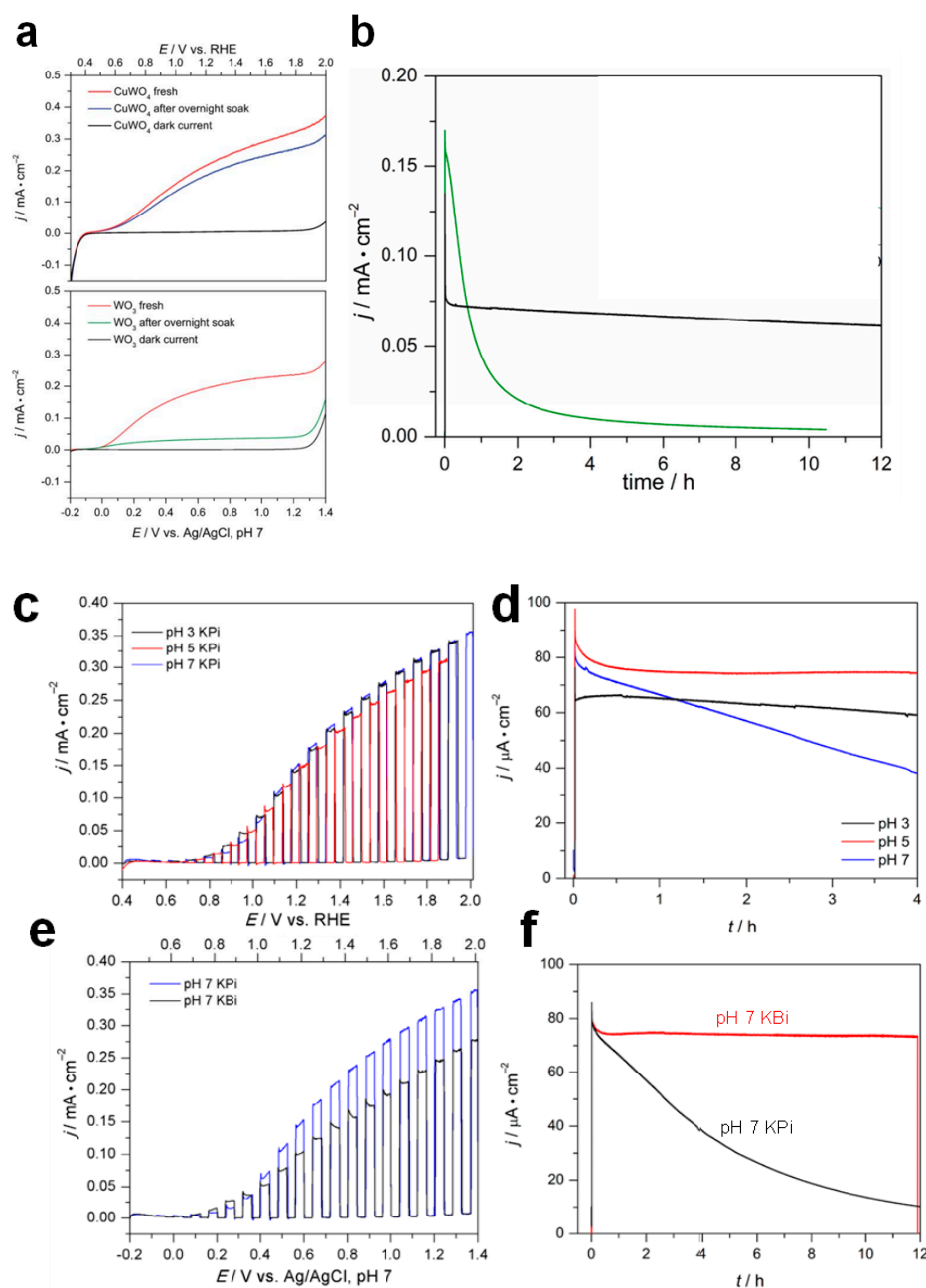


Figure 4. Stability of CuWO₄ photoanode in various conditions. (a) IV curves of CuWO₄ and WO₃. The blue and green traces show photocurrent density after soaking the electrodes in 0.1 M KPi overnight for CuWO₄ and WO₃, respectively. The photocurrent densities for both of the fresh photoanodes are shown in red. The black curves represent dark currents. (b) Chronoamperometry curves of water electrolysis with CuWO₄ (black) and WO₃ (green) at 0.5 V vs. Ag/AgCl in a 0.1 M phosphate buffer (pH 7). Reproduced from ref. [21]. CuWO₄ photoanode tested in different pHs (c,d) and electrolytes (e,f). (c,e) IV curves and (d,f) chronoamperometry with an applied potential of 1.23 V_{RHE}. All experiments were conducted under simulated AM 1.5G illumination (100 mW/cm²). Reproduced from ref. [33].

4. Photoelectrochemical Properties of CuWO₄ Photoanodes

As discussed in previous sections, CuWO₄ meets important criteria for being a suitable photoanode material to be used in aqueous electrolytes. As an n-type semiconductor, it has an appropriate electronic structure for hole-driven oxidation, with a VBM potential (2.85 V_{RHE}) deep enough to overcome the water oxidation redox potential (1.23 V_{RHE})

and a proper band bending at the semiconductor–electrolyte interface for smooth hole transfer [17]. Its inherent stability in near-neutral electrolytes under light irradiation warrants diverse applications involving hole oxidation.

Before the fabrication of a photoelectrode, it is good practice to test the photoactivity of the material in a simpler system, like photovoltaics or a photocatalyst. CuWO_4 was found to conduct photocatalytic water oxidation in an electron scavenger (Ag^+ or Fe^{2+})-containing solution, thus demonstrating that it is a good candidate material for a photoanode. Thus, Z. Wu et al. demonstrated that powder-type CuWO_4 showed n-type conductivity and the formation of a Schottky junction via contact potential difference (CPD) analysis, as well as photocatalytic water oxidation capability using an electron scavenger [34].

Studies of fundamental PEC properties indicated that thin films of CuWO_4 could successfully form a SCLJ. Mott–Schottky (MS) plots in various electrolytes confirmed n-type conductivity with a flat-band potential (E_{fb}) around $0.5 V_{RHE}$ and a quasi-Fermi level for the electron (E_{fn}) around $0.63 V_{RHE}$. The majority carrier density (N_D) from the slope of the MS plot was $\sim 10^{-19} \text{ cm}^{-3}$, which is comparable to that of BiVO_4 . The photovoltage (V_{ph}) of CuWO_4 was $\sim 0.6 \text{ V}$ without the electrocatalyst. The maximum V_{ph} can potentially reach 0.8 V if there is perfect interaction with $E_{fn} - E_{(O_2/H_2O)}$ with no Fermi level pinning. It is slightly lower than that of BiVO_4 ($0.05 V_{RHE} - 1.23 V_{RHE} = \sim 1.2 \text{ V}$) but comparable to that of Fe_2O_3 ($0.3 V_{RHE} - 1.23 V_{RHE} = 0.9 \text{ V}$) [26,35,36]. Besides establishing photovoltage at SCLJ, the formation of water oxidation intermediates at SCLJ was also confirmed in a similar manner to the cases of Fe_2O_3 and BiVO_4 [35].

A physical model for charge-carrier pathways in CuWO_4 under illumination is illustrated in Figure 5a—excitation, mid-gap state trapping, and charge–transfer reactions to the solution. The holes originating from VB possess the potential to directly participate in water oxidation or be localized in an intermediate state. The photoexcited electrons in CB move toward the F-doped SnO_2 (FTO) substrate, while some of them recombine with holes or migrate to the surface intermediates. The Nyquist plot for CuWO_4 demonstrates two independent charge transfer processes at the surface (Figure 5b). The semicircle known as RC1 is linked to non-Faradaic process in the depletion zone, represented as a parallel relationship between R_{trap} and C_{sc} , where R_{trap} is the resistance to trapping/detrapping electrons in/out of the mid-gap state, and C_{sc} is the capacitance of the space–charge region. Conversely, RC2 is related to a Faradaic reaction with the solution represented by $R_{ct,mg}$ and C_{mg} , where $R_{ct,mg}$ is the resistance to charge transfer at the surface/solution interface (to perform water oxidation) from the mid-gap state, and C_{mg} is the capacitance of the mid-gap state. As the applied voltage increases, the resistance associated with water oxidation ($R_{ct,mg}$) decreases, while the resistance associated with electron trapping (R_{trap}) increases. This behavior suppresses the recombination of photo-induced electrons at the mid-gap and facilitates electron transfer to the charge collector, initiating OER at 0.80 V . The capacitance of the space–charge region (C_{sc}) remains constant at potentials exceeding 0.86 V , indicating the continuous flow of electrons to the charge collector. In contrast, the capacitance of the mid-gap state (C_{mg}) continues to increase after 0.8 V , representing the charging and discharging of this state as water oxidation proceeds. The CuWO_4 showed a remarkable photocurrent increase and unpinning of the Fermi level at 1.06 V . This observation indicates that as the reaction proceeds, electrons from the solution populate the mid-gap state, and the increase in C_{mg} suggests that hole transfer from the valence band to the mid-gap state becomes rate limiting [37].

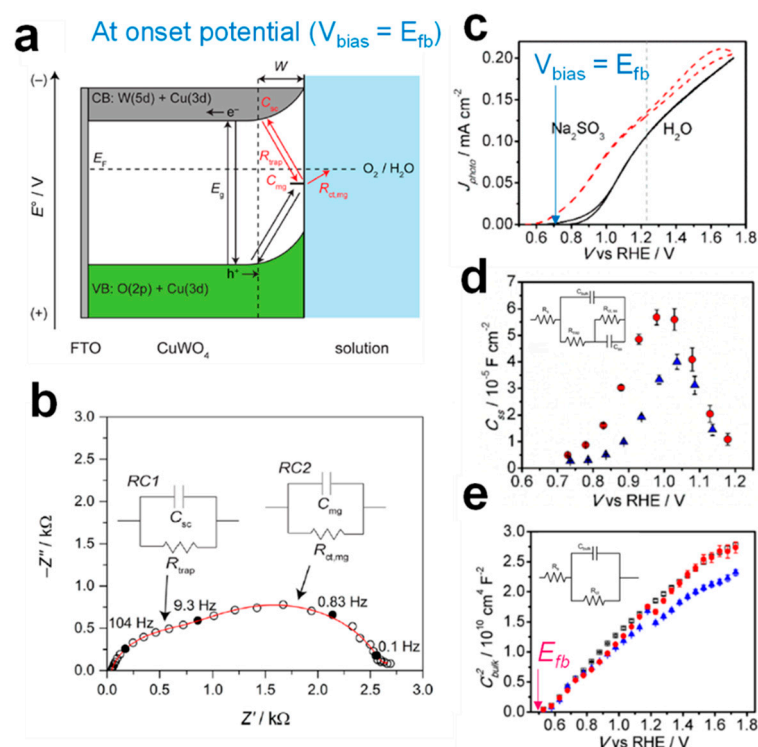


Figure 5. Formation of semiconductor–liquid junction for CuWO_4 in an aqueous electrolyte. (a) Proposed physical model for charge-carrier pathways in CuWO_4 : excitation, mid-gap state trapping, and charge-transfer reactions to solution. W represents the depletion width, and the red arrows indicate charge-transfer processes. (b) Nyquist plot for EIS data measured in 0.5 M KBi and 0.2 M KCl at pH 7, under one sun illumination, and $0.96 V_{\text{RHE}}$. Solid circles in Nyquist plot is marked with frequency of measurement applied to it. Reproduced from ref. [37]. (c) IV curves of CuWO_4/FTO in pH 9.0 KBi buffer under one sun illumination. (d) C_{ss} obtained via fitting EIS under 0.1 sun (blue triangles) and 1 sun (red circles) illumination in H_2O electrolyte, fitted with equivalent circuit for EIS data with two capacitive features (inset). (e) Mott–Schottky plots of CuWO_4 immersed in H_2O electrolyte, measured in the dark (open squares), under 0.1 sun (blue triangles) and 1 sun (red circles) illumination, fitted with a Randel circuit (inset). Reproduced from ref. [35].

The onset potentials of CuWO_4 for the PEC oxidation of water and Na_2SO_3 (a hole scavenger) were found to be around $0.85 V_{\text{RHE}}$ and $0.6 V_{\text{RHE}}$, respectively (Figure 5c). The observed shift in onset potential between the water and Na_2SO_3 oxidation processes is potentially due to the suboptimal hole collection during water oxidation at the CuWO_4 interface. The EIS analysis was conducted for CuWO_4 in H_2O and Na_2SO_3 solution to explain the observation. The derived surface state capacitance (C_{ss}) values diminished as the light intensity was reduced from 1 sun to 0.1 sun (Figure 5d). The peak C_{ss} at $\sim 1.0 V_{\text{RHE}}$ is close to its onset potential for water oxidation, while IV curves indicated that water oxidation intermediates form at $\sim 0.8 V_{\text{RHE}}$. Furthermore, the bulk capacitance (C_{bulk}) values decreased with the applied voltage, but they were essentially invariant at a given potential under different light intensities. Using these C_{bulk} values, MS plots were formulated in Figure 5e, which gave E_{fb} and N_{D} values comparable to the literature’s values, as described above [35].

Intensity modulated photocurrent spectroscopy (IMPS) was employed to quantify hole transfer kinetics at SCJL [35,38]. A large impedance of hole transfer at SCLJ turned out to be the major huddle of CuWO_4 for water oxidation, just like other known metal oxide semiconductors.

5. Modification Strategies of CuWO₄ Photoanodes

Despite having only recently emerged, the PEC water oxidation performance of CuWO₄ photoanodes has steadily improved through various modification strategies, as summarized in Table 1. These strategies include n-type doping, solid solution, heterojunction, electrocatalyst, and post-treatment, and each of these strategies is discussed in detail in this section.

Table 1. Summary of progress made for CuWO₄ as a photoanode material.

Strategies	Reported Substances	Typical Effects
Synthesis method	Electrodeposition [14,21] Thermal conversion [39,40] Sol-gel method [26,29,35] Hydrothermal [25]	Electrodeposition (J_{ph} 0.2 mA/cm ² at 1.23 V _{RHE}) [21]
	ALD [30] CVD [23] Ultrasonic spray pyrolysis [28] Impulse magnetron co-sputtering [32] PLD [31]	Thermal conversion (J_{ph} 0.33 mA/cm ² at 1.23 V _{RHE}) [24] Sol-gel (J_{ph} 0.5 mA/cm ² at 1.23 V _{RHE} , 1.0 mA/cm ² at 1.23 V _{RHE} for SA oxidation) [18] Sol-gel (J_{ph} 0.07 mA/cm ² at 1.23 V _{RHE} , 0.15 mA/cm ² at 1.23 V _{RHE} for SA oxidation) [26]
Doping	Fe ³⁺ [41] F [42] Y ³⁺ [43] Mo ⁶⁺ [44]	0.3% Fe:CuWO ₄ /FTO, ~1.5 times greater η_{bulk} (J_{ph} 0.5 mA/cm ² at 1.23 V _{RHE} for SA oxidation) [41]
Mo solid solution	Mo ⁶⁺ [45–48]	Red shift of photoresponse (from 550 nm to 600 nm) [45] CuW _{0.35} Mo _{0.65} O ₄ /FTO (J_{ph} 1.0 mA/cm ² at 1.23 V _{RHE} for SA oxidation) [46]
Heterojunction and electron transfer layer	WO ₃ (flat) [49] WO ₃ (nanorod) [39] WO ₃ (urchin like) [50] SnO ₂ [26] BiVO ₄ [51]	CuWO ₄ /flat WO ₃ /FTO. ~4 times increment (J_{ph} 0.55 mA/cm ² at 1.23 V _{RHE}) [49]
Electrocatalyst	Co-Pi [26,52,53] Co ₃ O ₄ [18] FeCoO _x [54] MnPO ₄ [55] NiWO ₄ [56] NiFeO _x [57] P-type sulfide (MoS ₂ , NbS ₂ , NiS _x) [44] MnNCN [58] Ni-Pi [59] Ag [60] IrCo-Pi [61]	Co-Pi/CuWO ₄ /FTO, 30% increment (J_{ph} 0.4 mA/cm ² at 0.6 V _{Ag/AgCl}) [52]
Post-treatment	H ₂ treatment [62]	H ₂ treatment (300 °C), 3-time increment (J_{ph} 0.6 mA/cm ² at 1.01 V _{Ag/AgCl}) [62]

SA: sacrificial agent. η_{bulk} = bulk charge separation efficiency.

5.1. Extrinsic/Intrinsic Defect Engineering via Doping

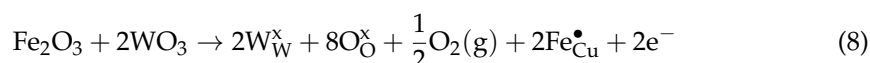
The extrinsic defect engineering conducted via the doping of foreign elements can promote the electron conductivity of CuWO₄ by generating additional charge carriers, which can be characterized using the MS equation.

$$\frac{1}{C^2} = \frac{2(V - E_{fb} - \frac{kT}{e})}{e\epsilon\epsilon_0 N_D A^2} \quad (7)$$

where C = the capacitance of the photoanode (metal oxide + electrolyte double layer, etc.), e = the charge of the electron, ϵ = the dielectric constant of CuWO₄, ϵ_0 = the permittivity of

the vacuum, V = the applied bias (vs. RHE), E_{fb} = the flat band potential (vs. RHE), k = the Boltzmann constant, N_D = the donor density of the n-type semiconductor (cm^{-3}), A = the surface area of photoanode, and T = the temperature (K). There are two kinds of doping methods: one uses a non-isovalent dopant, and the other uses an isovalent dopant. The non-isovalent dopants can enhance electron conductivity by elevating the charge-carrier density of CuWO_4 , while the isovalent doping also boosts conductivity by improving the charge migration, although it cannot enhance the charge density. The dopant atoms can substitute into Cu^{2+} or W^{6+} octahedral sites, and their efficacy is determined by their suitable oxidation state, ionic size, and electronic configuration.

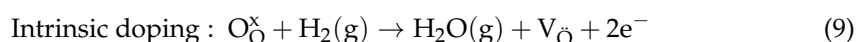
Fe doping was first applied to CuWO_4 as extrinsic doping via spray pyrolysis using a FeSO_4 precursor [41]. The iron was selected as a suitable dopant due to its prevalent non-toxic characteristics, its similarity in terms of the ionic radii of Fe^{3+} and Fe^{2+} to the target Cu^{2+} ion, and its good compatibility with the crystalline structure of CuWO_4 . The reaction (8) expresses the defect sites formed by Fe^{3+} substituting into the CuWO_4 lattice, as delineated by the Kröger–Vink notation:



The CuWO_4 doped with 0.3% Fe exhibited a 50% increase in photocurrent density compared to the undoped one at 1.23 V_{RHE} in 0.1 M KPi with an H_2O_2 hole scavenger. Furthermore, the charge separation efficiency at 1.23 V_{RHE} was 50% higher for the doped sample.

Yttrium was suggested as another extrinsic dopant by S. G. Poggini et al. [43]. Y-doping was conducted via a dip coating method. The Y-doping into CuWO_4 thin film led to a minor blue shift in the band gap from that of pristine CuWO_4 (2.30 eV) due to a rise in the conduction band position, as supported by DFT calculations. An optimized 5% Y-doped sample showed a photocurrent density 92.5% higher than that of an undoped sample at 1.3 V_{RHE} .

Another effective doping method for the CuWO_4 crystal lattice is to generate oxygen vacancies (V_O) through H_2 treatment, N_2 treatment, or F doping. The H_2 treatment increases the charge-carrier density through the partial reduction of the metal oxide:



Y. Tang et al. [62] conducted H_2 treatment for CuWO_4 to induce oxygen deficiency in its crystal lattice (Figure 6a,b). The H_2 -treated CuWO_4 film showed a noticeable color change from bright yellow to dark yellow as the annealing time increased because V_O can occur at a color center located in the band gap. This color change hints at a possible alteration in the CuWO_4 band gap caused by H_2 treatment. The UV–visible absorption spectra of bare and modified CuWO_4 samples shown in Figure 7a reflect this color change. The 30-min treatment gave the best performance, showing a negative shift of overpotential from 0.35 V to 0.05 V vs. Ag/AgCl, as well as an increased donor density in MS analysis compared to bare CuWO_4 (Figure 7b).

The use of nitrogen post-treatment to enhance the PEC performance of CuWO_4 by forming oxygen vacancy was suggested by Z. Ma et al. [63]. A nitrogen atmosphere can provide a moderate reductive environment for CuWO_4 , which neither collapses the crystal structure nor creates a color center in the band gap. As a result, there is no color change in the CuWO_4 films. The N_2 -treated CuWO_4 sample annealed at 623 K showed 80 $\mu\text{A}/\text{cm}^2$ @ 1.23 V_{RHE} in 0.1 M KPi under one sun illumination.

C. Li and P. Diao [42] introduced a straightforward method for fluorine doping, where F^- anions were substituted into the crystal lattice of CuWO_4 nanoflakes, replacing oxygen atoms and acting as potent electron donors to increase electron density. By modulating the volume of the F precursor solution, the dopant concentration was precisely controlled. The F-doped CuWO_4 nanoflakes demonstrated significantly enhanced PEC performance coupled with robust stability in PEC oxygen evolution reactions. The optimized 2.5%

F-doping enhanced the photocurrent density of CuWO_4 from 0.32 to 0.57 mA/cm^2 at 1.23 V_{RHE} .

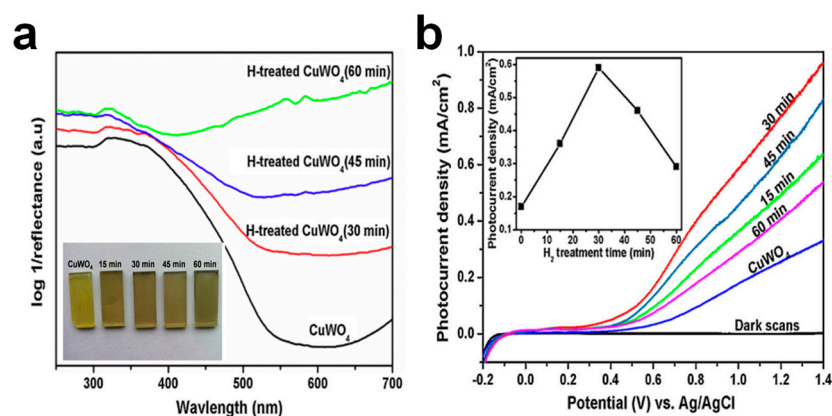


Figure 6. H_2 gas treatment for partial reduction of CuWO_4 photoanode. (a) UV-visible absorption spectra of CuWO_4 film with H_2 gas treatment (300°C , H_2 5%, Ar 95% flow) with different treatment durations. Inset is an image of a CuWO_4 film with H_2 gas treatment. (b) IV curves of CuWO_4 with H_2 gas treatment (0.1 M Na_2SO_4 , under simulated one sun). Inset represents the photocurrent densities at an applied bias of 1.01 $V_{\text{Ag}/\text{AgCl}}$. Reproduced from ref. [62].

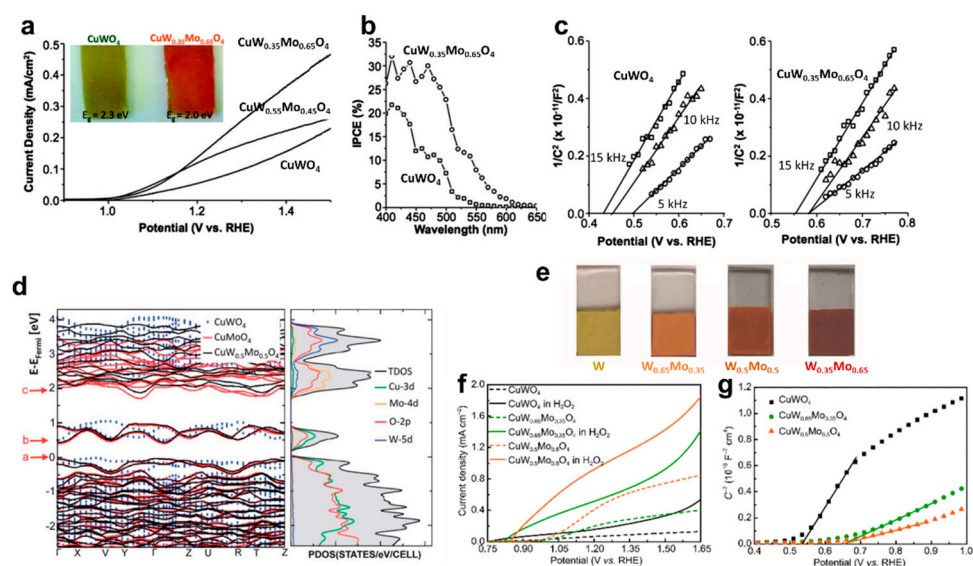


Figure 7. $\text{CuW}_{1-x}\text{Mo}_x\text{O}_4$ solid solution for photoanode. (a) IV curves of CuWO_4 and solid solutions ($W/\text{Mo} = 0.5/0.5$ and $0.35/0.65$) made via the electrodeposition (ED) of the precursor and thermal conversion (0.1 M KPi , pH 7.0, under simulated one sun). (b) IPCE under applied voltage of 1.61 V_{RHE} , (c) Mott-Schottky plots of CuWO_4 and $\text{CuW}_{0.35}\text{Mo}_{0.65}\text{O}_4$ obtained in 0.1 M KPi (pH 7), and (d) band structures of CuWO_4 , Type-III CuMoO_4 , and $\text{CuW}_{0.5}\text{Mo}_{0.5}\text{O}_4$ solid solutions, aligned by Mo (W) 4s, 4p (5s, 5p) core states (left) and projected density of states (PDOS) for a $\text{CuW}_{0.5}\text{Mo}_{0.5}\text{O}_4$ solid solution (right), obtained from DFT calculations (a: the Cu-O state, b: the Cu-O state with underestimated the local spin density approximation (LDA + U), c: the hybrid W/Mo 5d/4d and O 2p states). Reproduced from ref. [45]. (e) Images of $\text{CuW}_{1-x}\text{Mo}_x\text{O}_4$ film made via spray pyrolysis. (f) IV curves (0.1 M KPi pH 7.0, under simulated one sun, 0.1 mol% H_2O_2 as hole scavenger). (g) Mott-Schottky plots of $\text{CuW}_{1-x}\text{Mo}_x\text{O}_4$ film. Reproduced from ref. [46].

5.2. Formation of Solid Solution with Mo

Of the modification strategies developed to improve the PEC performance of CuWO_4 photoanodes, solid solution with Mo was the most effective and innovative [45,46,48].

The Mo^{6+} ion can easily replace W^{6+} in the CuWO_4 crystal structure because they have similar ionic radii and the same valance. The incorporation of Mo reduces the band gap and augments the light harvesting in the visible light region. The reduced band gap for $\text{CuW}_{1-x}\text{Mo}_x\text{O}_4$ is caused by the shift of the CBM to a low energy as Mo orbitals are mixed with Cu and W orbitals. This shift can push E_{fb} below the water reduction potential and make the overall water splitting impossible, but the PEC water oxidation efficiency improves significantly owing to extended light harvesting.

J. C. Hill et al. [45] demonstrated, for the first time, $\text{CuW}_{1-x}\text{Mo}_x\text{O}_4$ photoelectrode prepared using ED and thermal conversion methods. They identified an optimal photoelectrode of $\text{CuW}_{0.35}\text{Mo}_{0.65}\text{O}_4$ with a reddish color that showed the highest PEC performance (Figure 7a). To ascertain that the highest photocurrent comes from extended light harvesting, the incident photon-to-current conversion efficiency (IPCE) of CuWO_4 and $\text{CuW}_{0.35}\text{Mo}_{0.65}\text{O}_4$ are presented in Figure 7b. The photocurrent onset for CuWO_4 was 560 nm, whereas it shifted to 620 nm for $\text{CuW}_{0.35}\text{Mo}_{0.65}\text{O}_4$. This demonstrates that the increased photon absorption between 560 and 620 nm was directly translated into elevated photocurrents. In addition, $\text{CuW}_{0.35}\text{Mo}_{0.65}\text{O}_4$ showed substantially superior IPCEs across the entire visible light region. The MS plots of CuWO_4 and $\text{CuW}_{0.35}\text{Mo}_{0.65}\text{O}_4$ were displayed to discern their E_{fb} values (Figure 7c). Both samples exhibit marginal frequency-dependent variations, but on an aggregate scale, $\text{CuW}_{0.35}\text{Mo}_{0.65}\text{O}_4$ possesses a more positive E_{fb} than CuWO_4 . This implies that the augmented photocurrents of $\text{CuW}_{0.35}\text{Mo}_{0.65}\text{O}_4$ were caused by an increase in light absorption rather than E_{fb} . Moreover, the slopes of the MS plots for both samples appear similar at each frequency, suggesting that the E_{fb} was shifted by the CBM change rather than the variation in charge-carrier density. The band structures of CuWO_4 , Type-III CuMoO_4 , and $\text{CuW}_{0.5}\text{Mo}_{0.5}\text{O}_4$ solid solutions were calculated *via* DFT. The VBMs of all samples predominantly comprise hybridized Cu 3d and O 2p states. But the CBMs of $\text{CuW}_{0.5}\text{Mo}_{0.5}\text{O}_4$ and Type-III CuMoO_4 are mainly composed of hybridized Mo 4d and O 2p states, while the CBM of CuWO_4 consists of hybridized W 5d and O 2p states, as shown in Figure 7d.

Meanwhile, $\text{CuW}_{1-x}\text{Mo}_x\text{O}_4$ was synthesized via spray pyrolysis by Q. Liang et al. [46], who simply adjusted the ratio by adding an Mo source instead of a W source. As the Mo ratio increased, the color of $\text{CuW}_{1-x}\text{Mo}_x\text{O}_4$ changed to reddish, and when the Mo ratio was higher than 35%, $\text{Cu}_3\text{Mo}_2\text{O}_9$ impurity began to appear. Fortunately, the number of impurities was small up to 50% Mo content but increased rapidly beyond that level. These impurities can create a color center within the band and darken the color of $\text{CuW}_{1-x}\text{Mo}_x\text{O}_4$ samples (Figure 7e). The PEC performances of $\text{CuW}_{1-x}\text{Mo}_x\text{O}_4$ samples were measured in 0.1 M phosphate buffer with or without H_2O_2 under simulated one sun, and $\text{CuW}_{0.5}\text{Mo}_{0.5}\text{O}_4$ showed the best performance in both electrolytes. In water oxidation, it generated $\sim 0.47 \text{ mA/cm}^2$ at $1.23 V_{\text{RHE}}$ under one sun illumination, which was ~ 7 times higher than that of bare CuWO_4 . In H_2O_2 oxidation, $\text{CuW}_{0.5}\text{Mo}_{0.5}\text{O}_4$ recorded $\sim 0.95 \text{ mA/cm}^2$ at $1.23 V_{\text{RHE}}$, and its onset potential shifted by 80 mV in a cathodic direction due to the enhanced reaction kinetics (Figure 7f). The E_{fb} and charge density (N_{D}) of $\text{CuW}_{1-x}\text{Mo}_x\text{O}_4$ were calculated from MS plots, as shown in Figure 7g. $\text{CuW}_{0.65}\text{Mo}_{0.35}\text{O}_4$ and $\text{CuW}_{0.5}\text{Mo}_{0.5}\text{O}_4$ showed more positive E_{fb} than CuWO_4 , while N_{D} values estimated from the slopes of the MS plots were higher for bare CuWO_4 . The authors claimed that $\text{CuW}_{0.5}\text{Mo}_{0.5}\text{O}_4$ had enhanced conductivity and mitigated charge recombination.

A. Polo et al. [48] produced a $\text{CuW}_{0.5}\text{Mo}_{0.5}\text{O}_4$ photoelectrode by stacking layers using a spin coating method. They found that a three-layered sample was optimal, and using four or more layered samples led to electron mobility issues, reducing the performance. The three-layered $\text{CuW}_{0.5}\text{Mo}_{0.5}\text{O}_4$ generated a photocurrent of $\sim 0.25 \text{ mA/cm}^2$ at $1.23 V_{\text{RHE}}$ in 0.1 M K_3BO_3 , which was remarkably higher than CuWO_4 prepared via a similar method. Utilizing a similar spin coating method, K. Wang et al. [64] achieved a gradient distribution of Mo within the CuWO_4 film while doping the surface layer with Ni. The Mo incorporation caused the CBM to shift to a higher energy level, while the Ni doping induced the VBM to shift to a slightly lower energy, promoting efficient charge separation and alleviating

charge recombination. As a result, the fully modified CuWMoO₄ revealed 0.85 mA/cm² @ 1.23 V_{RHE}. Lastly, J. Yang et al. [47] made CuW_{1-x}Mo_xO₄ nanoflake films using hydrothermal and thermal solid-state reactions. They first synthesized Mo-WO₃ nanoflakes via a solid-state reaction, with desired amounts of Mo and W placed on the WO₃ seed layer. Then, a Cu precursor was deposited on it and heated to obtain a CuW_{1-x}Mo_xO₄ NFs film. The CuW_{0.68}Mo_{0.32}O₄ exhibited the best performance of ~0.62 mA/cm² at 1.23 V_{RHE} in 0.1 M sodium phosphate buffer solution.

5.3. Heterojunction Electron Transfer Layer

An effective heterojunction electron transfer layer (ETL) should possess the following characteristics: (i) enhanced electron transfer properties compared to CuWO₄, (ii) a type II staggered band alignment facilitating spontaneous electron transfer while blocking hole transfer, and (iii) a multidimensional high-aspect-ratio structure accompanied by porosity, enabling significant CuWO₄ loading while maintaining a modest thickness [65]. WO₃ has been commonly used as an ETL to improve the bulk charge separation efficiency for many photoanodes, such as Fe₂O₃ [66] and BiVO₄ [67], because it has an appropriate band gap (~2.7 eV), a high electron mobility (~10 cm²V⁻¹S⁻¹), and a long hole diffusion length (~800 nm) [68]. Moreover, the synthesis method of CuWO₄ from WO₃ is well known, and CuWO₄/WO₃ samples of various structures have also been reported.

D. Wang et al. [49] synthesized CuWO₄/WO₃ porous thin films through magnetron sputtering, employing a polymer templating approach. Utilizing a dip coating process, a Cu precursor with polymer surfactant was deposited on a WO₃ film. Then, CuWO₄/WO₃ was made via annealing at 550 °C for 2 h (Figure 8a). Figure 8b shows a cross-sectional SEM image of the CuWO₄/WO₃ composite, which clearly reveals respective WO₃ and CuWO₄ layers. The WO₃ seed layer became a little thinner as CuWO₄ of a thickness of 600 nm was formed. The CuWO₄/WO₃ composite exhibited a remarkably higher PEC performance of ~0.45 mA/cm² at 1.2 V_{RHE} compared to either the WO₃ or CuWO₄ photoanodes, as shown in Figure 8c. The IPCE for CuWO₄/WO₃ thin film at 1.2 V_{RHE}, as shown in Figure 8d, was much higher than those of the WO₃ and CuWO₄ films. Although CuWO₄ can absorb photons up to 540 nm, both samples revealed very low IPCEs between 470 and 540 nm, indicating that the charge carriers generated from CuWO₄ in this 470~540 nm range contribute little to the photocurrent generation. The CBs of CuWO₄ and WO₃ are positioned at +0.2 eV and +0.4 eV, respectively, whereas the VBs of CuWO₄ and WO₃ are positioned at +2.4 eV and +3.0 eV, respectively. When they form a CuWO₄/WO₃ heterojunction, the photo-induced holes from WO₃ migrate to CuWO₄, while electrons travel in the opposite direction to the FTO charge collector, as shown in Figure 8e.

T. Wang et al. [50] produced urchin-like nanoarray CuWO₄/WO₃ films through a one-step hydrothermal reaction by controlling the reaction time. The optimized CuWO₄/WO₃ nanoarray film demonstrated an onset potential of 0.6 V_{RHE} and a photocurrent density of 0.48 mA/cm² at 1.23 V_{RHE} in pH 7 solution. An enhanced PEC performance of the film can be attributed to its distinctive urchin-like nanoarray structure that provides a large surface area, in addition to facile charge separation by forming an effective CuWO₄/WO₃ heterojunction. I. Rodríguez-Gutiérrez et al. also synthesized CuWO₄/WO₃ photoelectrodes from WO₃ nanorod seed [39]. Through various electrochemical analyses, it was shown that WO₃ was partially or completely converted to CuWO₄, depending on the annealing temperature. It was found that only CuWO₄ was present in the sample that was annealed at temperatures of 650 °C or higher. However, the highest efficiency (~0.3 mA/cm² @ 1.23 V_{RHE} in 0.1 M phosphate buffer) was observed for the sample annealed at 450 °C, which contained a significant amount of WO₃. In addition, CuWO₄ served as a protective layer for the WO₃ material that is not generally stable in neutral aqueous solutions.

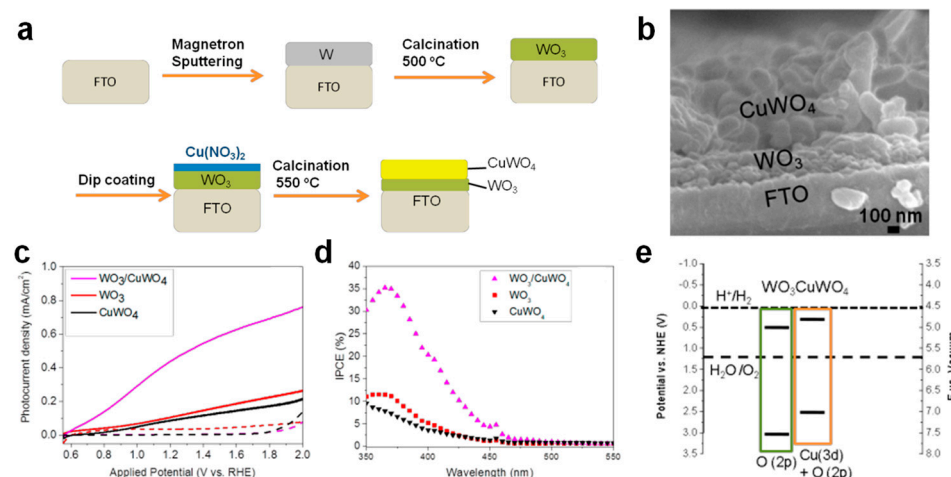


Figure 8. Effects of CuWO₄/WO₃ type II heterojunction. (a) Schematics of the formation of a CuWO₄/WO₃ heterojunction film and (b) its SEM image. (c) IV curves (solid line: under illumination, dotted line: under dark) and (d) IPCE at an applied bias of 1.20 V_{RHE} for CuWO₄, WO₃, and CuWO₄/WO₃ photoanodes in 0.5 M Na₂SO₄ under one sun. (e) Tentative energy diagram of the CuWO₄/WO₃ type II heterojunction based on UV-vis spectra and the Mott-Schottky plot. Reproduced from ref. [49].

Meanwhile, another common ETL material, namely SnO₂, was also applied to CuWO₄ film, which was synthesized via a spin coating method [26]. Although the CBM of SnO₂ is located at a higher energy than that of CuWO₄, its high electronic conductivity allows electrons to easily move to SnO₂, and the VBM of SnO₂ prevents the hole transfer from CuWO₄. As a result, the CuWO₄/SnO₂ sample showed a photocurrent of ~0.1 mA/cm² (at 1.23 V_{RHE} in 0.1 M KPi) and a bulk charge separation efficiency twice as high as that of bare at 1.23 V_{RHE}. The IPCE of CuWO₄/SnO₂ showed a diminished disparity in front/back side illumination conditions compared to bare CuWO₄. This suggests a more effective electron transfer for the CuWO₄/SnO₂ via the hole-blocking effect. In addition, SnO₂ ETL can inhibit the electron–hole recombination at the interface of the light absorber and charge collector.

5.4. Surface Modification via Co-Catalyst Loading

The surface modifications of CuWO₄ usually target the enhancement of charge transfer from a semiconductor to an electrolyte and stability under sun illumination. A simple but most effective way to modify the surface properties is to deposit an electrocatalyst on the semiconductor's surface. The electrocatalyst (termed co-catalyst on photoelectrode) plays multiple roles, such as (i) reducing the activation energy required for water oxidation, (ii) passivating the surface state or defects on the semiconductor, and (iii) storing photogenerated holes to promote a water oxidation reaction that requires multi-hole transfer [69]. The last two functions distinguish the co-catalyst on the photoanode from the typical electrocatalyst using only the first function.

A cobalt phosphate (Co-pi) is the best-known co-catalyst for oxygen evolution reaction (OER), as it is highly effective with various photoanodes. Figure 9a shows the band alignment and working mechanism when Co-Pi is loaded on CuWO₄. This scheme illustrates that Co-Pi effectively passivates the surface state of CuWO₄ to improve hole transfer efficiency and increase photovoltage [26,70]. S. Chen et al. [52] reported that Co-Pi could not induce a significant negative shift in the onset potential, but Co-Pi/CuWO₄ exhibited a higher photocurrent density than bare CuWO₄ by 86% at 1.23 V_{RHE} in 0.1 M KPi, as shown in Figure 9b. EIS data of bare CuWO₄ at 0.3 V_{RHE} were fitted into an equivalent circuit model comprising a single RC circuit related to the semiconductor–electrolyte interface (Figure 9c). In contrast, EIS data of Co-Pi/CuWO₄ aligned closely with an equivalent circuit model featuring two RC circuits. These circuits can be associated with the electron

transport between CuWO_4 and CoPi layers, as well as at the semiconductor–electrolyte interface. As a result, the Co-Pi/ CuWO_4 appears to enhance electron transfer both at the surface of CuWO_4 and within the electrode. The Co-Pi was introduced via various methods, such as cyclic voltammetry (CV) [53] and photo-assisted electrodeposition (PED) [26], and both methods formed an amorphous coating layer on a CuWO_4 particle. In addition, the Co-Pi/ CuWO_4 was more stable in electrolytes than bare CuWO_4 because the Co-Pi layer could cover the defects of the electrode surface and inhibit the charge accumulation on the surface.

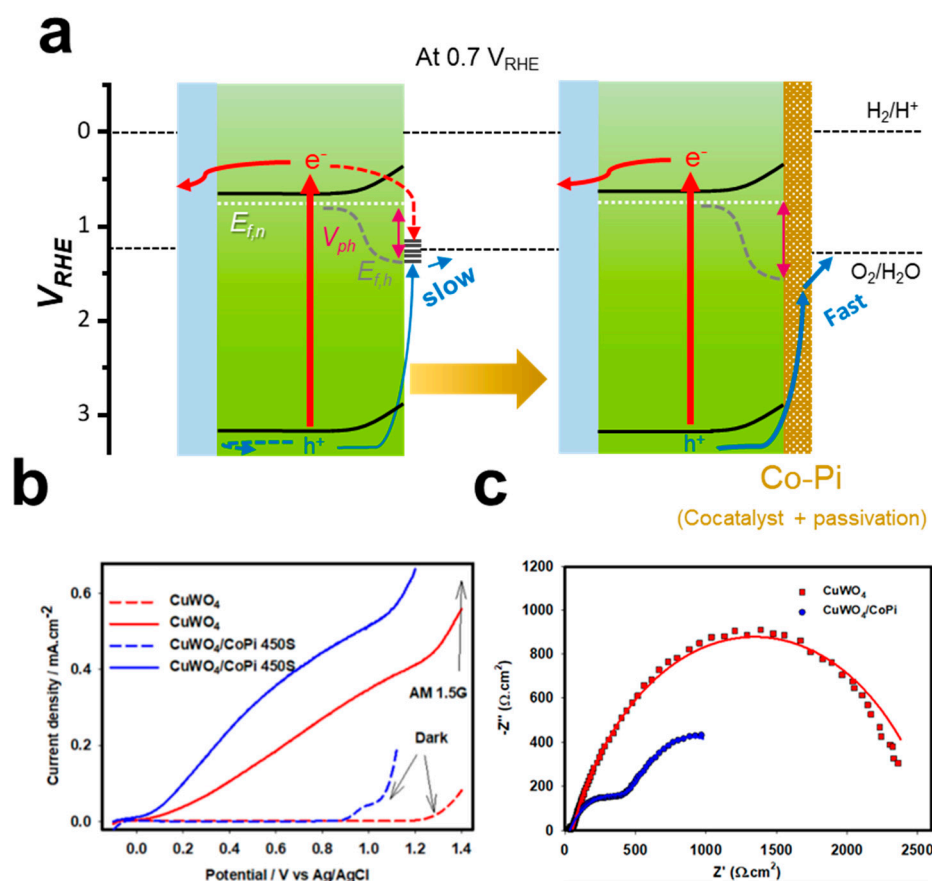


Figure 9. Efficacy of Co-Pi for CuWO_4 photoanode. (a) Working principle of CuWO_4 photoanodes with and without a Co-Pi co-catalyst. (b) IV curves and (c) Nyquist plots at an applied bias of 1.23 V_{RHE} in 0.1 M KPi, pH 7.0 under simulated one sun. Red and blue solid line are for from equivalent circuit. Reproduced from ref. [52].

Co_3O_4 was introduced by C. M. Tian et al. [35] as an OER co-catalyst that increased the surface charge separation efficiency by reducing the onset potential of CuWO_4 by ~ 100 mV. Through LSV and EIS analyses, however, they showed that too-thick co-catalyst layer created recombination sites where holes could not pass through, consequently leading to a decrease in PEC performance. The CuWO_4 can make the p-n junction with a p-type sulfide electrocatalyst [44]. This junction induced the photogenerated electron and hole transfer to the CuWO_4 bulk and p-type sulfide electrocatalyst, respectively. The photocurrent of the CuWO_4 /p-type sulfide increased and effectively reduced the onset potential by suppressing charge recombination. K. M. Nam et al. [55] compared Mn_2O_3 and MnPO co-catalysts in terms of enhancing the efficiency of a CuWO_4 photoanode. The OER catalytic performance of MnPO was relatively higher when it was applied to $\text{CuWO}_4/\text{WO}_3$ heterojunction. Unfortunately, the onset potential remained the same, but the stability and efficiency of MnPO/ $\text{CuWO}_4/\text{WO}_3$ increased to a reasonable extent. The NiWO_4 has a distorted wolframite crystal structure similar to CuWO_4 and can form a type

II heterojunction with CuWO_4 due to its higher energy CB and VB levels than those of CuWO_4 , reducing electron–hole recombination and improving IPCE [56]. P. Shadabipour et al. [57] deposited a well-known Ni- and Fe-based co-catalyst on CuWO_4 , but the OER efficiency of $\text{Ni}_{0.75}\text{Fe}_{0.25}\text{O}_y/\text{CuWO}_4$ did not significantly increase because photoexcited holes did not migrate efficiently and the reaction occurred preferentially on the CuWO_4 surface rather than on the co-catalyst.

The Ni-Pi synthesized on CuWO_4 via a drop-casting method dramatically increased the stability of CuWO_4 by interfering with charge accumulation [59]. In addition, it reduced charge recombination to greatly increase PEC performance. Moreover, the authors calculated the decay time of the charges in CuWO_4 and Ni-Pi/ CuWO_4 through a time-resolved photoluminescence (TRPL)-based approach and found that Ni-Pi/ CuWO_4 had a decay time of 400 μs , which was five times longer than that of bare CuWO_4 . M. Davi et al. [58] fabricated a MnNCN/ CuWO_4 electrode through ED and drop-casting. Interestingly, the surface of MnNCN converted to MnPO_x , forming a core–shell structure during water oxidation. However, the electrode showed a relatively small increase in activity, and the onset potential did not change. Noble metals were also introduced as co-catalysts for CuWO_4 . R. Salimi et al. [60] synthesized Ag-functionalized $\text{CuWO}_4/\text{WO}_3$ using a polyvinyl pyrrolidone (PVP)-assisted sol–gel (PSG) method. This photoanode showed a photocurrent of $\sim 0.2 \text{ mA}/\text{cm}^2$ at $1.23 V_{\text{RHE}}$ in 0.1 M phosphate buffer due to Ag functionalization, which enhanced charge transfer and separation efficiency and mitigated charge recombination. An IrCo-Pi co-catalyst was deposited on CuWO_4 NFs via the ED method to mitigate interfacial electron–hole recombination. The IrCo(9:1)-Pi/ CuWO_4 exhibited a photocurrent of $\sim 0.54 \text{ mA}/\text{cm}^2$ at $1.23 V_{\text{RHE}}$. Moreover, the co-catalyst-modified photoelectrode was more robust than bare CuWO_4 [61]. In conclusion, the strategy of co-catalyst has been studied in a variety of ways and is still being actively explored. Unfortunately, despite these research efforts, an optimized co-catalyst material that gives outstanding performance has not yet been found, which requires continued research.

6. Conclusions

CuWO_4 possesses a suitable band gap (2.3 eV) for solar water splitting, which positions it as a promising photoanode with a theoretical STH conversion efficiency exceeding 10%. Since its utilization as a photoanode began in 2011, the performance of CuWO_4 photoanodes has been steadily improved through advanced synthesis methods and modification strategies. The most noticeable event in the development of CuWO_4 photoanodes was the formation of a solid solution with Mo, thereby reducing the band gap to $\sim 2.1 \text{ eV}$, which resulted in a significant enhancement in solar light harvesting and water oxidation efficiency. In addition, modification strategies proven effective for other well-developed photoelectrodes have been applied to the CuWO_4 photoanodes. For example, forming a heterojunction with WO_3 or SnO_2 provides an ETL for effective charge transfer. Meanwhile, doping an M^{n+} ($n \geq 3$) ion into the Cu octahedral site or using gas treatment to generate oxygen vacancies increases the bulk charge-carrier density. Lastly, co-catalyst loading on CuWO_4 offers multiple benefits, such as increasing photovoltage, improving surface hole transfer kinetics, and enhancing chemical stability. A fundamental understanding of the CuWO_4 material and its working mechanism under PEC reaction conditions attained via DFT calculations and spectroscopy has facilitated these technical developments.

Despite these steady advancements, the performance of the CuWO_4 photoanodes still lags far behind the theoretical expectation. This shortfall comes from intrinsically undesirable PEC properties of CuWO_4 , like low charge separation efficiency, short hole diffusion length, sluggish surface kinetics, and low bulk conductivity. This signifies the pressing need for the development of an optimal synthesis method and effective modification strategies for CuWO_4 in the future. Additionally, strategies used to maximize efficiency by combining CuWO_4 with another photoanode with a smaller band gap or integrating it with a high-efficiency photocathode for overall water-splitting systems could also be pursued. The enhancement of CuWO_4 and its relevant variant will greatly enlarge

research and application opportunities (e.g., the commercialization of PEC solar overall water splitting) for solar energy utilization technology, just as BiVO₄ and Fe₂O₃ did for this field. For instance, future research, such as the valorization of organic molecular via partial oxidation, can be conducted using CuWO₄ and other tungstates, which will have different and interesting chemistry compared to those of other materials. Also, detailed analysis of the optoelectronic property of CuWO₄ will provide much information that is useful for solving the aforementioned problems realized in the current state of development. After this problem has been dealt with, CuWO₄ will surely be able to take the place of BiVO₄ due to its similarity in terms of operating conditions (near neutral) and elemental composition (ternary metal oxide), which will benefit the community studying photoelectrochemical cells in the same way as previous go-to materials. More specifically, owing to its appropriate band gap that can achieve STH above 10%, it can be possible candidate for a practical solar overall water-splitting PEC cell.

Author Contributions: Conceptualization, J.U.L. and J.H.K.; investigation, J.U.L.; data curation, J.H.K.; writing—original draft preparation, J.U.L. and J.H.K.; writing—review and editing, J.S.L.; supervision, J.H.K. and J.S.L.; project administration, J.H.K.; funding acquisition, J.S.L. All authors have read and agreed to the published version of the manuscript.

Funding: This work was supported by the Climate Change Response Project (NRF2019M1A2A2065612) and the Brainlink Project (NRF2022H1D3A3A01081140), funded by the Ministry of Science and ICT of Korea via National Research Foundation, and by research funds from Hanhwa Solutions Chemicals (2.220990.01) and UNIST (1.190013.01). This work was also supported by the Institute for Basic Science (IBSR019-D1). J.H.K. gratefully acknowledges the support from the Basic Science Research Program funded by the Ministry of Education (NRF2021R1A6A3A14039651, NRF-2019R1A6A3A01096197).

Data Availability Statement: Not applicable.

Conflicts of Interest: The authors declare no conflict of interest.

References

1. Davis, S.J.; Lewis, N.S.; Shaner, M.; Aggarwal, S.; Arent, D.; Azevedo, I.L.; Benson, S.M.; Bradley, T.; Brouwer, J.; Chiang, Y.-M.; et al. Net-zero emissions energy systems. *Science* **2018**, *360*, eaas9793. [[CrossRef](#)]
2. Lewis, N.S. Research opportunities to advance solar energy utilization. *Science* **2016**, *351*, aad1920. [[CrossRef](#)]
3. Jacobsson, T.J.; Fjällström, V.; Edoff, M.; Edvinsson, T. Sustainable solar hydrogen production: From photoelectrochemical cells to PV-electrolyzers and back again. *Energy Environ. Sci.* **2014**, *7*, 2056–2070. [[CrossRef](#)]
4. Yao, T.; An, X.; Han, H.; Chen, J.Q.; Li, C. Photoelectrocatalytic materials for solar water splitting. *Adv. Energy Mater.* **2018**, *8*, 1800210. [[CrossRef](#)]
5. Grätzel, M. Photoelectrochemical cells. *Nature* **2001**, *414*, 338–344. [[CrossRef](#)] [[PubMed](#)]
6. Mesa, C.A.; Francas, L.; Yang, K.R.; Garrido-Barros, P.; Pastor, E.; Ma, Y.; Kafizas, A.; Rosser, T.E.; Mayer, M.T.; Reisner, E.; et al. Multihole water oxidation catalysis on hematite photoanodes revealed by operando spectroelectrochemistry and DFT. *Nat. Chem.* **2020**, *12*, 82–89. [[CrossRef](#)] [[PubMed](#)]
7. Sivula, K.; Van De Krol, R. Semiconducting materials for photoelectrochemical energy conversion. *Nat. Rev. Mater.* **2016**, *1*, 15010. [[CrossRef](#)]
8. Walter, M.G.; Warren, E.L.; McKone, J.R.; Boettcher, S.W.; Mi, Q.; Santori, E.A.; Lewis, N.S. Solar Water Splitting Cells. *Chem. Rev.* **2010**, *110*, 6446–6473. [[CrossRef](#)]
9. Wang, Q.; Domen, K. Particulate Photocatalysts for Light-Driven Water Splitting: Mechanisms, Challenges, and Design Strategies. *Chem. Rev.* **2020**, *120*, 919–985. [[CrossRef](#)]
10. Kudo, A.; Miseki, Y. Heterogeneous photocatalyst materials for water splitting. *Chem. Soc. Rev.* **2009**, *38*, 253–278. [[CrossRef](#)]
11. Takata, T.; Jiang, J.; Sakata, Y.; Nakabayashi, M.; Shibata, N.; Nandal, V.; Seki, K.; Hisatomi, T.; Domen, K. Photocatalytic water splitting with a quantum efficiency of almost unity. *Nature* **2020**, *581*, 411–414. [[CrossRef](#)] [[PubMed](#)]
12. Sarnowska, M.; Bienkowski, K.; Barczuk, P.J.; Solarska, R.; Augustynski, J. Highly Efficient and Stable Solar Water Splitting at (Na)WO₃ Photoanodes in Acidic Electrolyte Assisted by Non-Noble Metal Oxygen Evolution Catalyst. *Adv. Energy Mater.* **2016**, *6*, 1600526. [[CrossRef](#)]
13. Park, Y.; McDonald, K.J.; Choi, K.-S. Progress in bismuth vanadate photoanodes for use in solar water oxidation. *Chem. Soc. Rev.* **2013**, *42*, 2321–2337. [[CrossRef](#)] [[PubMed](#)]
14. Hill, J.C.; Choi, K.-S. Synthesis and characterization of high surface area CuWO₄ and Bi₂WO₆ electrodes for use as photoanodes for solar water oxidation. *J. Mater. Chem. A* **2013**, *1*, 5006–5014. [[CrossRef](#)]

15. Bathula, B.; Eadi, S.B.; Lee, H.-D.; Yoo, K. ZnWO₄ nanorod-colloidal SnO₂ quantum dots core@shell heterostructures: Efficient solar-light-driven photocatalytic degradation of tetracycline. *Environ. Res.* **2023**, *228*, 115851. [[CrossRef](#)]
16. Babu, B.; Peera, S.G.; Yoo, K. Fabrication of ZnWO₄-SnO₂ Core-Shell Nanorods for Enhanced Solar Light-Driven Photoelectrochemical Performance. *Inorganics* **2023**, *11*, 213. [[CrossRef](#)]
17. Lhermitte, C.R.; Bartlett, B.M. Advancing the chemistry of CuWO₄ for photoelectrochemical water oxidation. *Acc. Chem. Res.* **2016**, *49*, 1121–1129. [[CrossRef](#)]
18. Tian, C.M.; Jiang, M.; Tang, D.; Qiao, L.; Xiao, H.Y.; Oropeza, F.; Hofmann, J.P.; Hensen, E.; Tadich, A.; Li, W.; et al. Elucidating the electronic structure of CuWO₄ thin films for enhanced photoelectrochemical water splitting. *J. Mater. Chem. A* **2019**, *7*, 11895–11907. [[CrossRef](#)]
19. Souza, E.L.S.; Szczancoski, J.C.; Nogueira, I.C.; Almeida, M.A.P.; Orlandi, M.O.; Li, M.S.; Luz, R.A.S.; Filho, M.G.R.; Longo, E.; Cavalcante, L.S. Structural evolution, growth mechanism and photoluminescence properties of CuWO₄ nanocrystals. *Ultrason. Sonochem.* **2017**, *38*, 256–270. [[CrossRef](#)]
20. Lalić, M.V.; Popović, Z.S.; Vukajlović, F.R. Ab initio study of electronic, magnetic and optical properties of CuWO₄ tungstate. *Comput. Mater. Sci.* **2011**, *50*, 1179–1186. [[CrossRef](#)]
21. Yourey, J.E.; Bartlett, B.M. Electrochemical deposition and photoelectrochemistry of CuWO₄, a promising photoanode for water oxidation. *J. Mater. Chem.* **2011**, *21*, 7651–7660. [[CrossRef](#)]
22. Lalić, M.V.; Popović, Z.S.; Vukajlović, F.R. Electronic structure and optical properties of CuWO₄: An ab initio study. *Comput. Mater. Sci.* **2012**, *63*, 163–167. [[CrossRef](#)]
23. Peeters, D.; Mendoza Reyes, O.; Mai, L.; Sadlo, A.; Cwik, S.; Rogalla, D.; Becker, H.W.; Schütz, H.M.; Hirst, J.; Müller, S.; et al. CVD-grown copper tungstate thin films for solar water splitting. *J. Mater. Chem. A* **2018**, *6*, 10206–10216. [[CrossRef](#)]
24. Hu, D.; Diao, P.; Xu, D.; Xia, M.; Gu, Y.; Wu, Q.; Li, C.; Yang, S. Copper (II) tungstate nanoflake array films: Sacrificial template synthesis, hydrogen treatment, and their application as photoanodes in solar water splitting. *Nanoscale* **2016**, *8*, 5892–5901. [[CrossRef](#)] [[PubMed](#)]
25. Zhang, Z.; Xiao, C.; Li, S. CuWO₄ films grown via seeding-hydrothermal method for photoelectrochemical water oxidation. *Mater. Lett.* **2018**, *232*, 25–28. [[CrossRef](#)]
26. Lee, J.U.; Kim, J.H.; Kang, K.; Shin, Y.S.; Kim, J.Y.; Kim, J.H.; Lee, J.S. Bulk and surface modified polycrystalline CuWO₄ films for photoelectrochemical water oxidation. *Renew. Energy* **2023**, *203*, 779–787. [[CrossRef](#)]
27. dos Santos Costa, M.J.; Lima, A.E.B.; Ribeiro, E.P.; dos Santos Costa, G.; Longo, E.; da Luz, G.E.; Cavalcante, L.S.; da Silva Santos, R. Transition metal tungstates AWO₄ (A²⁺ = Fe, Co, Ni, and Cu) thin films and their photoelectrochemical behavior as photoanode for photocatalytic applications. *J. Appl. Electrochem.* **2023**, *53*, 1349–1367. [[CrossRef](#)]
28. Duan, X.; Xu, C.; El Nahrawy, A.M.; Chen, J.; Zhu, Z.; Wang, J.; Liang, Q.; Cao, F. Ultrasonic Spray Pyrolysis-Assisted Fabrication of Ultrathin CuWO₄ Films with Improved Photoelectrochemical Performance. *ChemNanoMat* **2022**, *8*, e202100419. [[CrossRef](#)]
29. Gaillard, N.; Chang, Y.; DeAngelis, A.; Higgins, S.; Braun, A. A nanocomposite photoelectrode made of 2.2 eV band gap copper tungstate (CuWO₄) and multi-wall carbon nanotubes for solar-assisted water splitting. *Int. J. Hydrogen Energy* **2013**, *38*, 3166–3176. [[CrossRef](#)]
30. Gao, Y.; Zandi, O.; Hamann, T.W. Atomic layer stack deposition-annealing synthesis of CuWO₄. *J. Mater. Chem. A* **2016**, *4*, 2826–2830. [[CrossRef](#)]
31. Gonzalez, C.M.; Dunford, J.L.; Du, X.; Post, M.L. Characterization of carrier states in CuWO₄ thin-films at elevated temperatures using conductometric analysis. *J. Solid State Chem.* **2013**, *201*, 35–40. [[CrossRef](#)]
32. Hrubantova, A.; Hippler, R.; Wulff, H.; Cada, M.; Gedeon, O.; Jiricek, P.; Houdkova, J.; Olejnicek, J.; Nepomniashchaia, N.; Helm, C.A.; et al. Copper tungsten oxide (Cu_xWO_y) thin films for optical and photoelectrochemical applications deposited by reactive high power impulse magnetron co-sputtering. *J. Appl. Phys.* **2022**, *132*, 215301. [[CrossRef](#)]
33. Yourey, J.E.; Pyper, K.J.; Kurtz, J.B.; Bartlett, B.M. Chemical stability of CuWO₄ for photoelectrochemical water oxidation. *J. Phys. Chem. C* **2013**, *117*, 8708–8718. [[CrossRef](#)]
34. Wu, Z.; Zhao, Z.; Cheung, G.; Doughty, R.M.; Ballesteros-Barrientos, A.R.; Hirmez, B.; Han, R.; Maschmeyer, T.; Osterloh, F.E. Role of Surface States in Photocatalytic Oxygen Evolution with CuWO₄ Particles. *J. Electrochem. Soc.* **2019**, *166*, H3014. [[CrossRef](#)]
35. Gao, Y.; Hamann, T.W. Elucidation of CuWO₄ surface states during photoelectrochemical water oxidation. *J. Phys. Chem. Lett.* **2017**, *8*, 2700–2704. [[CrossRef](#)]
36. Mayer, M.T. Photovoltage at semiconductor–electrolyte junctions. *Curr. Opin. Electrochem.* **2017**, *2*, 104–110. [[CrossRef](#)]
37. Pyper, K.J.; Yourey, J.E.; Bartlett, B.M. Reactivity of CuWO₄ in photoelectrochemical water oxidation is dictated by a midgap electronic state. *J. Phys. Chem. C* **2013**, *117*, 24726–24732. [[CrossRef](#)]
38. Gao, Y.; Hamann, T.W. Quantitative hole collection for photoelectrochemical water oxidation with CuWO₄. *Chem. Commun.* **2017**, *53*, 1285–1288. [[CrossRef](#)]
39. Rodríguez-Gutiérrez, I.; Djatoubai, E.; Rodríguez-Pérez, M.; Su, J.; Rodríguez-Gattorno, G.; Vayssieres, L.; Oskam, G. Photoelectrochemical water oxidation at FTO|WO₃@CuWO₄ and FTO|WO₃@CuWO₄|BiVO₄ heterojunction systems: An IMPs analysis. *Electrochim. Acta* **2019**, *308*, 317–327. [[CrossRef](#)]
40. Peng, B.; Li, C.; Yue, C.; Diao, P. Sacrificial Template Synthesis of Copper Tungstate: Influence of Preparing Conditions on Morphology and Photoactivity. *Int. J. Electrochem. Sci.* **2019**, *14*, 2574–2588. [[CrossRef](#)]

41. Bohra, D.; Smith, W.A. Improved charge separation via Fe-doping of copper tungstate photoanodes. *Phys. Chem. Chem. Phys.* **2015**, *17*, 9857–9866. [[CrossRef](#)] [[PubMed](#)]
42. Li, C.; Diao, P. Fluorine doped copper tungsten nanoflakes with enhanced charge separation for efficient photoelectrochemical water oxidation. *Electrochim. Acta* **2020**, *352*, 136471. [[CrossRef](#)]
43. González-Poggini, S.; Sánchez, B.; Colet-Lagrange, M. Enhanced Photoelectrochemical Activity of CuWO₄ Photoanode by Yttrium Doping. *J. Electrochem. Soc.* **2023**, *170*, 066512. [[CrossRef](#)]
44. Ikeue, K.; Ueno, T. Photoelectrochemical water oxidation properties of Mo-doped CuWO₄: Effect of p-type sulfide loading and annealing. *Mater. Lett.* **2023**, *348*, 134690. [[CrossRef](#)]
45. Hill, J.C.; Ping, Y.; Galli, G.A.; Choi, K.-S. Synthesis, photoelectrochemical properties, and first principles study of n-type CuW_{1-x}Mo_xO₄ electrodes showing enhanced visible light absorption. *Energy Environ. Sci.* **2013**, *6*, 2440–2446. [[CrossRef](#)]
46. Liang, Q.; Guo, Y.; Zhang, N.; Qian, Q.; Hu, Y.; Hu, J.; Li, Z.; Zou, Z. Improved water-splitting performances of CuW_{1-x}Mo_xO₄ photoanodes synthesized by spray pyrolysis. *Sci. China Mater.* **2018**, *61*, 1297–1304. [[CrossRef](#)]
47. Yang, J.; Li, C.; Diao, P. Molybdenum doped CuWO₄ nanoflake array films as an efficient photoanode for solar water splitting. *Electrochim. Acta* **2019**, *308*, 195–205. [[CrossRef](#)]
48. Polo, A.; Nomellini, C.; Grigioni, I.; Dozzi, M.V.; Selli, E. Effective Visible Light Exploitation by Copper Molybdo-Tungstate Photoanodes. *ACS Appl. Energy Mater.* **2020**, *3*, 6956–6964. [[CrossRef](#)]
49. Wang, D.; Bassi, P.S.; Qi, H.; Zhao, X.; Gurudayal; Wong, L.H.; Xu, R.; Sritharan, T.; Chen, Z. Improved Charge Separation in WO₃/CuWO₄ Composite Photoanodes for Photoelectrochemical Water Oxidation. *Materials* **2016**, *9*, 348. [[CrossRef](#)]
50. Wang, T.; Fan, X.; Gao, B.; Jiang, C.; Li, Y.; Li, P.; Zhang, S.; Huang, X.; He, J. Self-Assembled Urchin-like CuWO₄/WO₃ Heterojunction Nanoarrays as Photoanodes for Photoelectrochemical Water Splitting. *ChemElectroChem* **2021**, *8*, 125–134. [[CrossRef](#)]
51. Ye, W.; Chen, F.; Zhao, F.; Han, N.; Li, Y. CuWO₄ nanoflake array-based single-junction and heterojunction photoanodes for photoelectrochemical water oxidation. *ACS Appl. Mater. Interfaces* **2016**, *8*, 9211–9217. [[CrossRef](#)]
52. Chen, S.; Hossain, M.N.; Chen, A. Significant enhancement of the photoelectrochemical activity of CuWO₄ by using a cobalt phosphate nanoscale thin film. *ChemElectroChem* **2018**, *5*, 523–530. [[CrossRef](#)]
53. Li, C.; Guo, B.; Peng, B.; Yue, C.; Diao, P. Copper Tungstate (CuWO₄) Nanoflakes Coupled with Cobalt Phosphate (Co-Pi) for Effective Photoelectrochemical Water Splitting. *Int. J. Electrochem. Sci.* **2019**, *14*, 9017–9029. [[CrossRef](#)]
54. Rosa, W.S.; Rabelo, L.G.; Tiveron Zampaulo, L.G.; Gonçalves, R.V. Ternary Oxide CuWO₄/BiVO₄/FeCoO_x Films for Photoelectrochemical Water Oxidation: Insights into the Electronic Structure and Interfacial Band Alignment. *ACS Appl. Mater. Interfaces* **2022**, *14*, 22858–22869. [[CrossRef](#)] [[PubMed](#)]
55. Nam, K.M.; Cheon, E.A.; Shin, W.J.; Bard, A.J. Improved Photoelectrochemical Water Oxidation by the WO₃/CuWO₄ Composite with a Manganese Phosphate Electrocatalyst. *Langmuir* **2015**, *31*, 10897–10903. [[CrossRef](#)] [[PubMed](#)]
56. Fan, L.; Sunarso, J.; Zhang, X.; Xiong, X.; He, L.; Luo, L.; Wang, F.; Fan, Z.; Wu, C.; Han, D.; et al. Regulating the hole transfer from CuWO₄ photoanode to NiWO₄ electrocatalyst for enhanced water oxidation performance. *Int. J. Hydrogen Energy* **2022**, *47*, 20153–20165. [[CrossRef](#)]
57. Shadabipour, P.; Raithel, A.L.; Hamann, T.W. Charge-Carrier Dynamics at the CuWO₄/Electrocatalyst Interface for Photoelectrochemical Water Oxidation. *ACS Appl. Mater. Interfaces* **2020**, *12*, 50592–50599. [[CrossRef](#)]
58. Davi, M.; Mann, M.; Ma, Z.; Schrader, F.; Drichel, A.; Budnyk, S.; Rokicinska, A.; Kustrowski, P.; Dronskowski, R.; Slabon, A. An MnNCN-Derived Electrocatalyst for CuWO₄ Photoanodes. *Langmuir* **2018**, *34*, 3845–3852. [[CrossRef](#)]
59. Xiong, X.; Fan, L.; Chen, G.; Wang, Y.; Wu, C.; Chen, D.; Lin, Y.; Li, T.; Fu, S.; Ren, S. Boosting water oxidation performance of CuWO₄ photoanode by surface modification of nickel phosphate. *Electrochim. Acta* **2019**, *328*, 135125. [[CrossRef](#)]
60. Salimi, R.; Sabbagh Alvani, A.A.; Mei, B.T.; Naseri, N.; Du, S.F.; Mul, G. Ag-Functionalized CuWO₄/WO₃ nanocomposites for solar water splitting. *New J. Chem.* **2019**, *43*, 2196–2203. [[CrossRef](#)]
61. Li, C.; Diao, P. Boosting the Activity and Stability of Copper Tungsten Nanoflakes toward Solar Water Oxidation by Iridium-Cobalt Phosphates Modification. *Catalysts* **2020**, *10*, 913. [[CrossRef](#)]
62. Tang, Y.; Rong, N.; Liu, F.; Chu, M.; Dong, H.; Zhang, Y.; Xiao, P. Enhancement of the photoelectrochemical performance of CuWO₄ films for water splitting by hydrogen treatment. *Appl. Surf. Sci.* **2016**, *361*, 133–140. [[CrossRef](#)]
63. Ma, Z.; Linnenberg, O.; Rokicinska, A.; Kustrowski, P.; Slabon, A. Augmenting the Photocurrent of CuWO₄ Photoanodes by Heat Treatment in the Nitrogen Atmosphere. *J. Phys. Chem. C* **2018**, *122*, 19281–19288. [[CrossRef](#)]
64. Wang, K.; Chen, L.; Liu, X.; Li, J.; Liu, Y.; Liu, M.; Qiu, X.; Li, W. Gradient surficial forward Ni and interior reversed Mo-doped CuWO₄ films for enhanced photoelectrochemical water splitting. *Chem. Eng. J.* **2023**, *471*, 144730. [[CrossRef](#)]
65. Kim, J.H.; Lee, J.S. Elaborately modified BiVO₄ photoanodes for solar water splitting. *Adv. Mater.* **2019**, *31*, 1806938. [[CrossRef](#)] [[PubMed](#)]
66. Sivula, K.; Formal, F.L.; Grätzel, M. WO₃-Fe₂O₃ Photoanodes for Water Splitting: A Host Scaffold, Guest Absorber Approach. *Chem. Mater.* **2009**, *21*, 2862–2867. [[CrossRef](#)]
67. Shi, X.; Zhang, K.; Shin, K.; Ma, M.; Kwon, J.; Choi, I.T.; Kim, J.K.; Kim, H.K.; Wang, D.H.; Park, J.H. Unassisted photoelectrochemical water splitting beyond 5.7% solar-to-hydrogen conversion efficiency by a wireless monolithic photoanode/dye-sensitised solar cell tandem device. *Nano Energy* **2015**, *13*, 182–191. [[CrossRef](#)]
68. Bignozzi, C.A.; Caramori, S.; Cristino, V.; Argazzi, R.; Meda, L.; Tacca, A. Nanostructured photoelectrodes based on WO₃: Applications to photooxidation of aqueous electrolytes. *Chem. Soc. Rev.* **2013**, *42*, 2228–2246. [[CrossRef](#)]

69. Wang, D.; Li, R.; Zhu, J.; Shi, J.; Han, J.; Zong, X.; Li, C. Photocatalytic Water Oxidation on BiVO₄ with the Electrocatalyst as an Oxidation Cocatalyst: Essential Relations between Electrocatalyst and Photocatalyst. *J. Phys. Chem. C* **2012**, *116*, 5082–5089. [[CrossRef](#)]
70. Nellist, M.R.; Qiu, J.; Laskowski, F.A.; Toma, F.M.; Boettcher, S.W. Potential-sensing electrochemical AFM shows CoPi as a hole collector and oxygen evolution catalyst on BiVO₄ water-splitting photoanodes. *ACS Energy Lett.* **2018**, *3*, 2286–2291. [[CrossRef](#)]

Disclaimer/Publisher's Note: The statements, opinions and data contained in all publications are solely those of the individual author(s) and contributor(s) and not of MDPI and/or the editor(s). MDPI and/or the editor(s) disclaim responsibility for any injury to people or property resulting from any ideas, methods, instructions or products referred to in the content.